TECHNISCHE HOCHSCHULE MITTELHESSEN

CAMPUS GIESSEN

EI Elektro- und Informationstechnik

JLU NEUE WEGE. SEIT 1607.

JUSTUS-LIEBIG-UNIVERSITÄT GIESSEN

Bachelor Thesis

Calibration of Sensors for Attitude Determination on CubeSats for Optical Inter-Satellite Links

Simon Spier

December 2022

PTRA

BACHELOR THESIS

Title

Calibration of Sensors for Attitude Determination on CubeSats for Optical Inter-Satellite Links

submitted by

Simon Spier

in cooperation with

Institute for Communication and Navigation, German Aerospace Center (DLR), Oberpfaffenhofen

Date:	January 17, 2023
Course:	B. Sc. Physics and Technology for Space Applications
Matriculation Number:	5013797 (JLU), 5298697 (THM)
Reviewer:	Prof. Dr. Chris Volkmar
Second Reviewer:	Dr. Kristof Holste
Supervisor DLR:	René Rüddenklau

Contents

List of Figures

List of Tables

List of Abbreviations

4QPD .... Four-Quadrant Photodiode
ADC .... Analog-to-Digital Converter
ADCS .... Attitude Determination and Control System
COTS .... Commercial-off-the-Shelf
CPA .... Coarse Pointing Assembly
CubeISL .... CubeSat Inter-Satellite Links
DLR .... Deutsches Zentrum für Luft- und Raumfahrt e.V. / German Space Agency
DGRF .... Definitive Geomagnetic Reference Field
DTO .... Direct-To-Earth
ECEF .... Earth Centered Earth Fixed
ECI .... Earth Centered Inertial
ESA .... European Space Agency
FoV .... Field of View
FPA .... Fine Pointing Assembly
FSM .... Fine Steering Mirror
FSO .... Free Space Optical
GSOC .... German Space Operations Center
IAGA .... International Association of Geomagnetism and Aeronomy
IGRF .... International Geomagnetic Reference Field
JLU .... Justus Liebig University Giessen
KN-OP .... Institute for Communication and Navigation, Oberpfaffenhofen
LEO .... Low Earth Orbit
LSM .... Least Squares Method
MEMS .... Micro-Electro Mechanical Systems

MI .... Magneto-Inductive

MR .... Magneto-Resistive

NED .... North-East-Down

OGS .... Optical Ground Station

OGSE .... Optical Ground Support Equipment

OSIRIS .... Optical Space Infrared Downlink System

OSL .... Optical Satellite Links

PCB .... Printed Circuit Board

RF .... Radio Frequency

RMM .... Residual Magnetic Moments

THM .... Technische Hochschule Mittelhessen / Technical College of Central Hesse

WMM .... World Magnetic Model

Abstract

This thesis describes calibration routines for inertial measurement units, namely two gyroscopes and one magnetometer, used in the CubeISL project at the German Aerospace Center. Optimizing optical inter-satellite links, a promising technology in the rapidly growing CubeSat sector, is the project's primary goal. Due to the investigated algorithms, the sensors will provide precise attitude information and ensure a faster and more stable optical communication link acquisition.

Calibration of the gyroscopes occurs in a lab environment. The results show a valuable decrease in cross-axis sensitivity and functional scaling. Determination of the sensor bias increases the stability of the calculated angles to gain more meaningful relative attitude information. Finally, the calibration results in the lab environment are verified with an optical link. Thus, mounting differences between the attitude sensors and the four-quadrant diode sensor are also resolved and analyzed. Magnetic disturbances in the lab environment impede verification, so tests outdoors are conducted. Both implemented algorithms work well in different scenarios and increase the sensor's performance. Further analysis must be executed in the future to determine the superior choice. All examined algorithms are suitable for on-orbit calibration, allowing the flexible compensation of errors caused by heavy loads during launch.

Chapter 1. Motivation

The Institute for Communication and Navigation (KN-OP) at the German Aerospace Center (DLR) has been researching optical data transfer via lasers for a long time. In 2007, the groundwork for examining this technology in space was laid when the project OSIRIS was started. With its first missions, the satellites OSIRIS v2 (launched 2016), OSIRIS v1 (launched 2017) and OSIRIS v3 (not yet launched), the technology proved efficient and worth investigating to broaden the possibilities of satellite communication.[1][2] Generally, a greater demand for satellite communication requires enhanced data throughput. Free Space Optical (FSO) communication is essential for improving data transfer as the established Radio Frequency (RF) communication is limited in data rates. With the narrow beam divergence of lasers, a drastically increased data rate can be achieved without consuming more power [3].

A vital part of the communication hardware is the laser terminal. With the system's successful miniaturization, the DLR can keep pace with the rapidly growing CubeSat market. In the context of the project OSIRIS4CubeSat, implementation of the small laser terminal called CubeLCT[1] has already been achieved on the satellite PIXL-1 in cooperation with the German company TESAT. The satellite was launched in January of 2021 and is the first satellite using Commercial-Off-The-Shelf (COTS) components operated by the German Space Operations Center (GSOC)[4][3]. As the satellites get smaller, it also gets easier and cheaper to deploy many of them at once. Using COTS components also provides more affordable solutions by not relying on space-grade materials that must endure a lengthy testing process[2]. These factors not only offer excellent opportunities for students and startups[5] to develop their own satellites but also open up the possibility of creating commercial satellite constellations like Starlink by SpaceX or OneWeb [6]. The Starlink constellation is planned to consist of at least 12 000 satellites with active laser communication between them. Four optical links per satellite are assumed in the conception of the constellation.[7]

Thus, such communication between satellites, so-called *Optical Inter-Satellite Links* (OSL), will be a vast field of study in the future. The project focusing on this topic at the DLR is called *CubeISL*, an acronym describing inter-satellite links on CubeSats. Each CubeSat is therefore equipped with a laser to send a beacon or data and a receiver for incoming laser beams. Lasers with a small divergence consume less power and are profitable for the link budget. Direct-To-Earth (DTO) scenarios benefit from unlimited power availability and can send a beacon beam with a wide divergence covering the satellite's position uncertainty area. Limited in power consumption, a satellite can only provide a minor beam divergence. To utilize the narrow beam divergence and still ensure a stable link, a motorized and regulated system on the receiving end is implemented, effectively increasing the observable area. The Fine Pointing Assembly (FPA) consists of a Fine Steering Mirror (FSM) already in use and a Coarse Pointing

1 `https://satsearch.co/products/tesat-cubelct` (viewed last on 08.01.2023)
2 See for example standard MIL-STD-883 by the US Department of Defense: `http://everyspec.com/MIL-STD/MIL-STD-0800-0899/MIL-STD-883L_56323/` (viewed last on 02.01.2023)

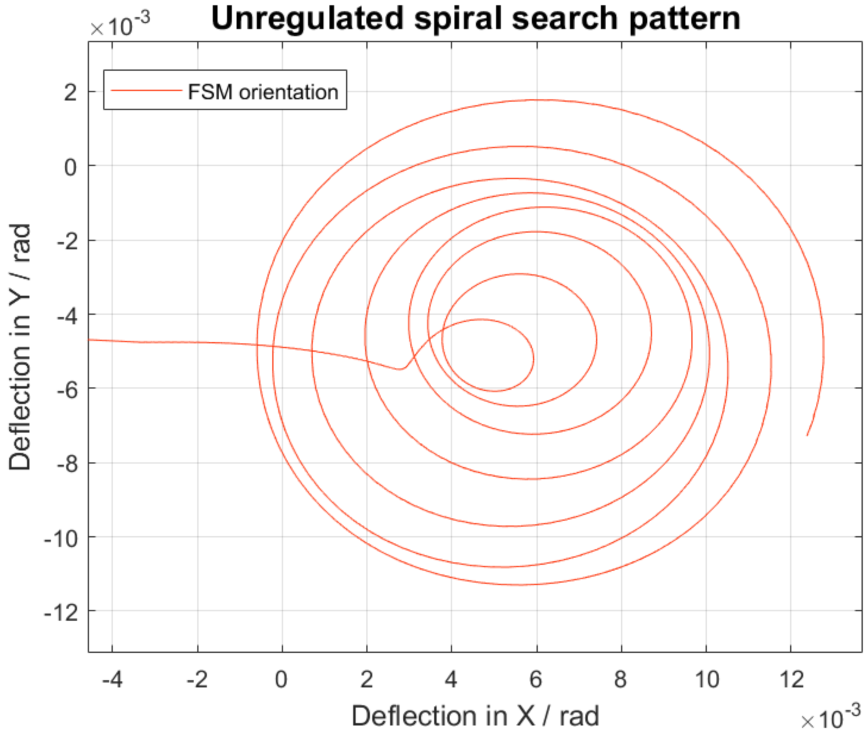

Figure 1.1.: The simulation of a distorted spiral search pattern is shown by depicting the FSM's deflection in X and Y. Such distortions stem from infrequent attitude updates and result in spacious unobserved areas endangering link acquisition.

Assembly (CPA) currently in development. Considering the control loop, a Four-Quadrant Photodiode (4QPD) provides information about the beam's centricity. Therefore, the mirror can adjust accordingly to account for any small, unforeseen satellite movement and ensure a stable link. The complete acquisition concept of the project is described in detail in [3].

A spiraling search pattern guarantees finding the laser beam in the first place. The mirror thus traverses an area of radius 1° around the center. This is taking into account the pointing accuracy[3] reached by the satellite's Attitude Determination and Control System (ADCS) and the 4QPD sensor's Field of View (FoV). Figure 1.1 shows a simulation of the spiral search pattern distorted by unaccounted satellite movements. Large unobserved spaces result from the pattern's deformation and endanger the link acquisition. Decreasing the spiral radius increment ensures obtaining a link but results in less available communication time.

In order to account for the satellite's motion, the control loop requires attitude information, which is only available once per second from the ADCS. Since the optics system needs to adjust to changes much faster than with a rate of 1 Hz, the mirror control loop repeats at least with a 200 Hz frequency. Even a 1 kHz control loop frequency seems feasible in future generations. If attitude information by additional sensors is available at such high rates, the spiral pattern can be regulated considering the satellite movement as depicted in figure 1.2. Both pictures stem from simulations in the project's early phases, determining the feasibility of the solution. Note that the spiral's center is not located at zero due to the simulation of an offset and not the

3 See: `https://gomspace.com/6u-standard.aspx` (viewed last on 02.01.2023)

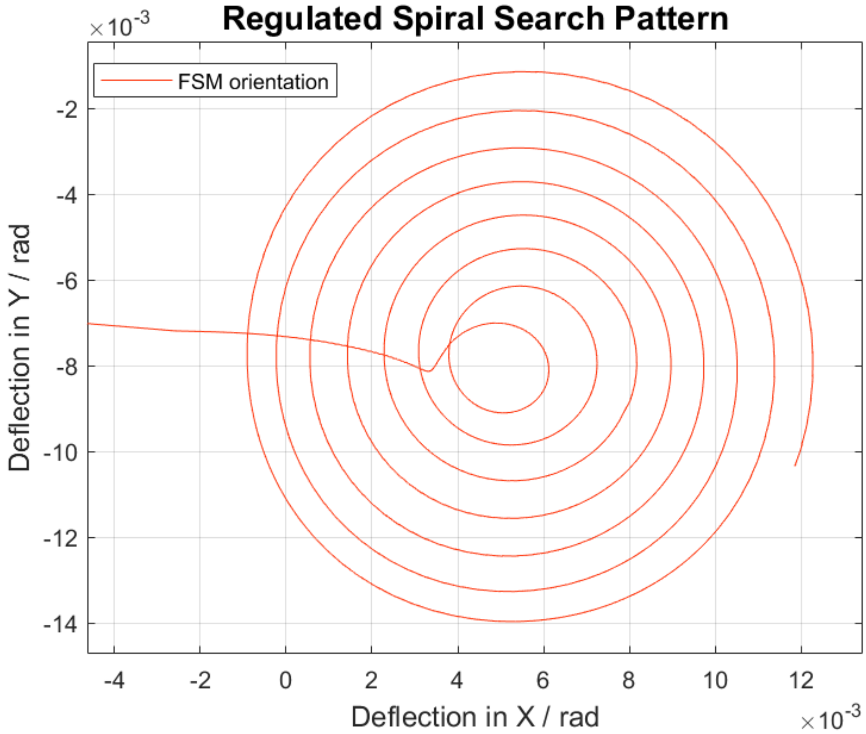

Figure 1.2.: This simulation presents the benefits of supplementary sensors. The additional attitude information is used to prevent distortions, and a functional link acquisition is ensured.

maximum radius 1° equaling about 17.45 mrad is depicted for simplicity.

During the one second of the satellite's control loop, it is subject to disturbances inducing a tumbling motion. Torques influencing the attitude of a satellite stem from aerodynamic forces, gravity gradients, solar radiation forces and magnetic disturbances. Aerodynamic torques come up as the center of mass differs from the center of pressure. Since the hull of a spacecraft is not homogeneous, the solar pressure acts differently on the various features, creating torque. Gravity is a fundamental physics force subject to a $1/r^2$ decline and dependent on the mass distribution of the evoking body. Therefore, the strength of the gravitational force acting on a three-dimensional object differs and can cause torques. Finally, as Bangert showed in chapter 3.1 of [8], the interaction between the Earth's magnetic field and the satellite's Residual Magnetic Moment (RMM) creates a dipole, which is the most influential factor to consider. The other influences can be neglected since CubeSats are tiny.

So, the satellite is tumbling; hence, gaining better attitude information more quickly is an important goal to account for any satellite movements during the slow control loop of the satellite's main bus. Gaining the angular velocity information from a gyroscope sensor allows relative attitude estimation by propagating the measurements from the last known attitude. Magnetic field measurements can be used to determine the absolute attitude of a spacecraft, but at least two independent sensors are necessary for that. Due to confinements considering the payload's size, weight and power (SWaP), only one magnetometer has been implemented. Therefore, new solutions to determine the absolute attitude with only this limited amount of available data will be investigated in the project's future.

Before using the sensors for their dedicated purpose of providing fast and reliable attitude information, they have to be calibrated to ensure the correctness of the measurements. As large mechanical loads during launch can change sensor parameters and introduce new errors, on-orbit calibration algorithms must be employed to guarantee a successful mission. Therefore, this thesis focuses on calibration algorithms for a magnetic field sensor and a gyroscope implemented on the prototype of the CubeISL terminal.

At first, the theoretical background will be explained, focusing on mathematical concepts of attitude and physical principles of angular velocity and the earth's magnetic field. Then, the functionality of the sensors will be introduced, and the calibration algorithms will be addressed in the second half of chapter 2. Chapter 3 focuses on the results of the first simulations conducted to determine the feasibility of the algorithms. This will be complemented by chapter 4 presenting the results of hardware tests conducted in the laboratory. Lastly, a conclusion will be formulated in chapter 5.

Chapter 2. Theory

Theories about vector geometry (section 2.1), magnetism (section 2.3), sensor types (section 2.4), and sensor calibration (section 2.5) are essential for testifying the simulation and understanding the conducted experiments.

A general remark considering mathematical notation: Matrices will be denoted by bold, capital characters like $\boldsymbol{M}$, and the matrix's dimension will be explained by the text commenting on the equation. Vectors $\vec{v}$ are depicted as letters with a superscript arrow and are usually three-dimensional, meaning a particular case of a matrix with dimensions 3×1. Vectors can be either capital or lower-case letters, depending on context. For example, the magnetic flux density $\vec{B}$ is usually written with a capital letter, whereas the lower case $\vec{\omega}$ is typically used for the angular velocity.

2.1. Coordinate Systems and Attitude

As explained in chapter 1, the concept of having magnetic field sensors and gyroscopes on the satellite is to gain knowledge of the satellite's attitude. Therefore, the definition of coordinate systems and attitude representations is crucial to investigate.

2.1.1. Coordinate Systems

The attitude is described mathematically by two Cartesian coordinate systems: The *body frame* and the reference coordinate system. While the body system is fixed at the center of the satellite or in a sensor, the reference system changes with the attitude and lies outside of the object.

Different reference coordinate frames are standard in aerospace applications. The *Earth Centered Inertial* (ECI) coordinate system originates in the center of mass of Earth. It uses the Spring Point to define the x-axis and the North Pole for the z-axis, while *Earth Centered Earth Fixed* (ECEF) uses the intersection of the meridian and equator for its x-axis. Here, the z-axis is also defined by the north pole, and the y-axis is defined by opening a right-handed system with the other two axes (chapter 4.5.3.1 of [9]). The third frequently used coordinate system in aerospace applications is fixed to the satellite's orbit and called the *North-East-Down* (NED) frame. While the x-axis points parallel to the Earth's surface in the polar direction (North), the y-axis is defined eastward along the latitude curve, and the z-axis always aims toward the Earth's center (Down). To represent the attitude of a body, a rotation matrix has to be found describing the difference between both coordinate systems. Direction-Cosine matrices are the easiest way to relate two coordinate frames but are challenging to read and understand (chapter 4.5.3.2 of [9]). Instead, Euler angles are preferred to describe rotations.

2.1.2. Euler Angles

Euler angles are suited well to describe angular movements around different axes. According to chapter 4.5.3.3, in [9], the rotations around the standard axes x, y and z can be described as in equations 2.1, 2.2 and 2.3 respectively.

$$\boldsymbol{R_x}(\varphi) = \begin{bmatrix} 1 & 0 & 0 \\ 0 & \cos\varphi & -\sin\varphi \\ 0 & \sin\varphi & \cos\varphi \end{bmatrix} \tag{2.1}$$

$$\boldsymbol{R_y}(\theta) = \begin{bmatrix} \cos\theta & 0 & \sin\theta \\ 0 & 1 & 0 \\ -\sin\theta & 0 & \cos\theta \end{bmatrix} \tag{2.2}$$

$$\boldsymbol{R_z}(\psi) = \begin{bmatrix} \cos\psi & -\sin\psi & 0 \\ \sin\psi & \cos\psi & 0 \\ 0 & 0 & 1 \end{bmatrix} \tag{2.3}$$

φ corresponds to the rotation about the x-axis, which is usually called *roll* in flight scenarios. θ and ψ make up the y- or *pitch*- axis and the z- or *yaw*-axis, respectively. A generalized version of these rotation matrices can be determined by multiplying all three equations. The matrix multiplication results in the matrix depicted in equation (2.4). Note that the matrix depends on the multiplication sequence.

$$R(\varphi,\theta,\psi) = \begin{bmatrix} c_\theta c_\psi & s_\varphi s_\theta c_\psi - c_\varphi s_\psi & c_\varphi s_\theta c_\psi + s_\varphi s_\psi \\ c_\theta s_\psi & s_\varphi s_\theta s_\psi + c_\varphi c_\psi & c_\varphi s_\theta s_\psi - s_\varphi c_\psi \\ -s_\theta & s_\varphi c_\theta & c_\varphi c_\theta \end{bmatrix} \tag{2.4}$$

Here, standard shorthand notation $s_\alpha \equiv \sin\alpha$ and $c_\alpha \equiv \cos\alpha$ is used. A problem with Euler angles is the existence of a singularity when only using three parameters to describe the attitude. This can result in a so-called gimbal lock, as explained in chapter 5.8 of [10]. To avoid this, a quaternion representation of the attitude is often used.

2.1.3. Quaternions

Quaternions are mathematical number systems extending the complex numbers first described by William Rowan Hamilton in 1843. The typical imaginary i is extended by two more complex representations, j and k. A quaternion may look like equation (2.5) with a, b, c and d being real numbers and i, j and k being the imaginary descriptors. In vector notation, $\vec{q}$ is of dimension 4×1 with the real part $a = q_0$ and the imaginary parts condensed in a 3×1 vector $\vec{q}_{1:3}$.

$$\begin{gathered} q = a + bi + cj + dk \\ \vec{q}_{4\times1} = [a,b,c,d]^T = \left[q_0, \vec{q}_{1:3}\right]^T \end{gathered} \tag{2.5}$$

Therefore, quaternions are four-dimensional, eliminating the singularity of the Euler angles and making visualization and physical interpretation even more complicated. Due to this problem, quaternions are primarily utilized in on-board- and post-processing. For other purposes, the Euler angles are calculated from the quaternion representation of the attitude. The satellite's ADCS also uses quaternions and provides them to the payload microcontroller. Further explanation will be omitted here as quaternions are not essential for the calibration but only for the implementation later in the project.

2.1.4. Attitude Determination

Attitude Determination is a crucial step in any satellite mission regarding pointing cameras, antennas and sensing equipment toward the Earth. Other applications, such as the alignment of solar arrays, also need reliable orientation information. As explained in chapter 1.3 of [11], two forms of attitude determination, *relative* and *absolute*, have to be distinguished. With relative attitude estimation, sometimes referred to as *inertial guidance*, the angular velocity of a rigid body and a previous orientation is known. Propagation of the movement then provides an estimation of the actual attitude. Since the rate has to be integrated, minor errors accumulate, making periodic absolute orientation updates necessary. On the other hand, an absolute attitude determination algorithm estimates the orientation without any previous knowledge. The attitude can be estimated with reference information and a measurement of the same entity. In three-dimensional space, at least two measurements are required, for example, a sun sensor and a magnetic field sensor. Other sources of reference attitude information can also be found in table 1-1 of [11].

Grace Wahba laid the theoretical groundwork for absolute attitude determination by proposing the so-called *Wahba's problem* in 1965 specifically for satellite attitude estimation [12].

$$L(\boldsymbol{A}) = \sum_i a_i |\vec{b}_i - \boldsymbol{A}\vec{r}_i|^2 \tag{2.6}$$

Equation (2.6) shows the mathematical formulation of the problem where $L(\boldsymbol{A})$ has to be minimized considering $\boldsymbol{A}$. Requiring $\boldsymbol{A}$ to be an attitude matrix, the condition of $\det \boldsymbol{A} = +1$ is introduced. The sets of unit vectors $\vec{b}_i$ and $\vec{r}_i$ represent measurements in the satellite's body frame and the corresponding vectors in the reference frame, respectively. Mathematical notation differs slightly from the original formulation as it is taken from [13], where a weight factor a_i is introduced for each measurement. This equation is similar to the error function of a least squares problem as introduced later in equation (2.23) in section 2.5.1 and needs at least two sets of vectors to be solvable. Many algorithms have since been developed, some providing accurate analytical results, while numerical algorithms often benefit from faster solutions with less computational effort. A comparison of practical algorithms can be found in [13].

2.2. Angular Velocity

Angular velocity is determined by deriving an angle with respect to time. Thus, the development of the mathematical background for rotations is equivalent to the theory of linear motion. This is shown in equation (2.7), where ω is the angular velocity, φ is the angle, and t is the time. The discrete formulation can be found in section 2.3.2 of [14] while the continuous representation is used in Chapter 8.1 of [15].

$$\omega = \frac{\Delta\varphi}{\Delta t} \quad \rightarrow \quad \lim_{\Delta t \rightarrow 0} \omega = \frac{\partial\varphi}{\partial t} = \dot{\varphi} \tag{2.7}$$

Therefore, a constant angle yields an angular velocity of zero since it does not change. Deriving the angular rate with respect to time again produces the angular acceleration. While a lower case ω usually denotes the angular velocity, in some literature, the capital Ω is also used. The angular velocity around all three Cartesian axes can be determined, resulting in a three-dimensional vector.

Since different units exist for angles, angular velocity can also appear in different units, mainly the SI unit representation $\mathrm{rad\,s^{-1}}$. As a non-SI unit describing angles, degree (°) is popular and easier to visualize than fractions of pi. The conversion of the units is calculated as follows in equation (2.8).

$$\frac{\varphi}{^\circ} = \frac{180}{\pi} \cdot \frac{\varphi}{\mathrm{rad}} \tag{2.8}$$

Notation for degrees per second varies in the literature (e.g. $^\circ\,\mathrm{s}^{-1}$ or dps), but since the data sheets of both gyroscopes implemented on the terminal use dps, it will be used in this thesis as well. In attitude determination applications, the angular velocity can only be utilized to gain *relative* attitude information by propagating the movement.

2.3. Magnetism

2.3.1. General Concepts

Magnetic fields are one of the most basic physical phenomena and have been thoroughly investigated and used for a long time. Still, some questions remain on the properties of magnetic fields and their origin, as Demtröder points out in the introduction to chapter 3 of [16]. In general, magnetic fields are created by magnetized material or moving charges. The magnetization of a material can be traced back to moving charges and magnetic moments on an atomic scale. A magnetic field also can influence moving electric charges and currents via, for example, the Lorentz force and can interact with magnetic materials.

$$\vec{F}_L = q\left(\vec{E} + \vec{v} \times \vec{B}\right) \tag{2.9}$$

Equation (2.9) shows the definition of the Lorentz force with $\vec{F}_L$ being the force. The vectors $\vec{E}$, $\vec{v}$ and $\vec{B}$ describe the electric field, the velocity of the particle and the magnetic flux density, respectively, while q is the charge of said particle. $\vec{E}$ and $\vec{B}$ both being part of the equation indicate the close connection of magnetic fields and electric fields through Maxwell's equations. Therefore, magnetism is part of the electromagnetic force, one of the four fundamental forces of nature. Bécherrawy explains various details of magnetism and Maxwell's equations in chapters 6, 7 and 9 of [17], but they shall be omitted here as the basics are sufficient for this thesis.

The wording around the quantity of a magnetic field is sometimes challenging as two closely related values have to be distinguished. $\vec{H}$ is a vector representing the magnetic field strength with unit $\mathrm{A\,m^{-1}}$. The magnetic field strength is connected to the magnetic flux density via a factor depending on the material and magnetization. For a linear and isotropic medium, the factor can be assumed constant.

$$\vec{B} = \mu_0(\vec{H} + \vec{M}) = \mu_0(1 + \chi_M)\vec{H} = \mu_0\mu_r\vec{H} = \mu\vec{H} \tag{2.10}$$

Equation (2.10) shows the relation between both variables, where $\vec{B}$, $\vec{H}$ and $\vec{M}$ are the magnetic flux density, the external magnetic field strength and the magnetization, respectively. $\mu_0 = 4\pi 10^7 \mathrm{V\,s\,A^{-1}\,m^{-1}}$ is the constant vacuum permeability and χ_M is the magnetic susceptibility of the material. As the magnetization is also subject to $\vec{H}$, the value μ_r is a relative factor depending on the material and external magnetic field strength. μ_r is an entity of the dimension number. The two factors are reduced by defining a new factor μ as the product of μ_0 and μ_r. The unit of the magnetic flux density is Tesla (T).

Measuring a magnetic field is usually achieved by measuring the forces it produces. Equation (2.9) shows that the force depends on the flux density $\vec{B}$, and it is, therefore, the entity usually used to quantify the magnetic field. Distinguishing the part originating from $\vec{M}$ and $\vec{H}$ is challenging and not required for most applications. Due to this, the magnetic flux density is often described as the *magnetic field strength*. In a purely physical context, this should be considered incorrect. Still, as the magnetic flux density is usually used to quantify the magnetic field, the descriptors are used interchangeably in this thesis.

2.3.2. Earth's Magnetic Field

Planet Earth is surrounded by a relatively strong magnetic field, preventing charged particles of solar winds from hitting the surface and enabling humans to navigate via compasses. The most significant part of the field is generated by liquid iron in Earth's outer core, called the *core field*. In addition, magnetic material in the ground and electric currents in the seawater generate local aberrations to the field. External components may also evoke field deviations. These can be caused by time-varying electric currents in the atmosphere, which induce currents in the ground and oceans. External magnetic fields like this are considered *disturbance fields*. These sources of Earth's magnetic field are further explained in the paper describing the current iteration of the World Magnetic Model (WMM) [18].

Considering the dynamic nature of Earth's magnetic field, it is clear that it varies with time. Many satellite missions have been conducted to measure the magnetic field, and algorithms have been implemented to model the magnetic field for the past and the near future. The most prominent models in use are the WMM [18] and the International Geomagnetic Reference Field (IGRF) [19]. Both models output a vector with seven elements describing the geomagnetic field. The first three components represent the intensity in the NED coordinate system, which is commonly used in aviation. X, Y, and Z are defined in northerly, easterly and vertical (positive downwards) directions, respectively. Four additional variables are also calculated by the models. Thus, the horizontal intensity H as in equation (2.11), the total intensity F as in equation (2.12), the inclination angle I as in equation (2.12) and the declination angle D as in equation (2.14) extend the vector.

$$H = \sqrt{X^2 + Y^2} \tag{2.11}$$

$$F = \sqrt{X^2 + Y^2 + Z^2} = \sqrt{H^2 + Z^2} \tag{2.12}$$

$$I = \arctan \frac{Z}{H} \tag{2.13}$$

$$D = \arctan \frac{Y}{Z} \tag{2.14}$$

X, Y, Z, H and F are values of unit nT with $1\,\mathrm{T} = 1\,\mathrm{kg\,s^{-2}\,A^{-1}}$. The angles I and D are calculated in radians but can be easily converted into degrees using equation (2.8). Gauss coefficients have been determined for both models, which can be interpolated for a specific time and place. Then, Schmidt semi-normalized Legendre polynomials $P_n^m(\cos\theta)$ of degree n and order m are calculated recursively. The theoretical background of Schmidt quasi-normalization is well-described in [20] and will not be further explained here.

Equation (2.15) shows the calculation of the scalar magnetic potential specifically for the IGRF model, where a approaches the mean Earth radius with 6 371 200 m, but is called the geomagnetic reference radius. The radial distance from the Earth's center is denoted by r, θ describes the geocentric co-latitude, and ϕ is the longitude.

$$V(r,\theta,\phi,t) = a \sum_{n=1}^{N} \sum_{m=0}^{n} \left(\frac{a}{r}\right)^{n+1} \left[g_n^M(t) \cos m\phi + h_n^m(t) \sin m\phi\right] P_n^m \cos\theta \tag{2.15}$$

Deriving the potential outputs the magnetic field strength according to equation 2.16.

$$\vec{B}(r,\theta,\phi,t) = -\nabla V(r,\theta,\phi,t) \tag{2.16}$$

In this, $\vec{B}$ is the time-dependent magnetic field in spherical coordinates, ∇ is the derivative operator vector, and V is the scalar potential calculated in equation (2.15). To gain the Cartesian NED coordinates explained earlier, the values must be converted as described in section 1.2 of [18]. Furthermore, the IGRF-13 model covers an extensive period. As a Definitive Geomagnetic Reference Field (DGRF), the modeled magnetic field from 1900 to 2015 is finally determined. For the epoch 2015-2020, the magnetic field is modeled already, but the coefficients may be adapted in a future generation to describe it better. The essential epoch for this work is the current epoch ranging from 2020 to 2025, in which the model predicts the magnetic field strength considering previous measurements. In comparison, the WMM is only designed to model the specific time frame of 2020-2025. Since both models work similarly and yield similar results, but the IGRF is more extensive, this work focuses on the IGRF model; specifically, the current iteration IGRF-13 [19].

By calculating a reference value of the magnetic field at a specific time and location and measuring the magnetic field vector in the same position, both vectors can be compared. The information gained by the comparison can help determine the attitude of the body coordinate system of the sensor; thus, the satellite attitude can also be estimated. Therefore, an *absolute* attitude determination is feasible with magnetic field measurements.

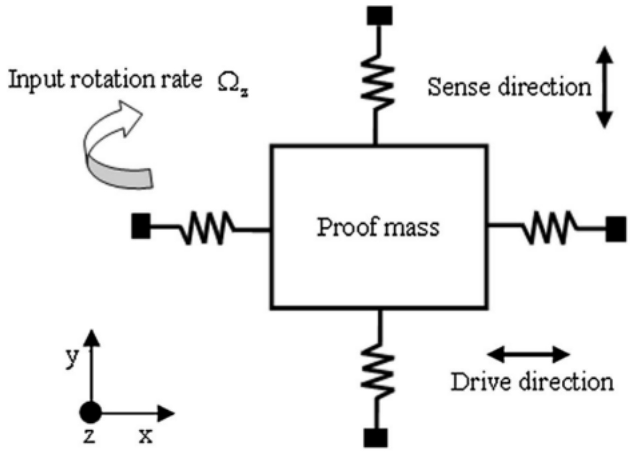

Figure 2.1.: Mechanics model of a MEMS gyroscope explained in @[21]. A rotation around the z-axis results in a Coriolis force in the y-direction due to the lateral motion of the driven oscillation in the x-direction.

2.4. Sensors

2.4.1. Gyroscope Sensor

A gyroscope sensor (*gyroscope* for short) is a sensor measuring angular velocity. Different methods and types of angular velocity sensors exist. Note that rotating devices that can maintain an orientation due to the conservation of angular momentum are also called gyroscopes but will not be the subject of this thesis.

In the project's conception phase, two sensors were chosen for implementation. The IAM-20380 from TDK InvenSense[1] and the A3G4250 by ST Microelectronics[2]. Both sensors are vibratory Micro-Electro Mechanic Systems (MEMS) rate gyroscopes detecting rotations around the x-, y- and z-axes. A lateral motion in a rotating reference frame evokes a *Coriolis effect*. Therefore, as depicted in equation (2.17) and explained in [21], the Coriolis force is applied on a proof weight and springs, resulting in a vibrating motion. Here, $\vec{F}_C$ denotes the Coriolis force and m the proof mass. Finally, $\vec{\Omega} \times \vec{v}$ is the cross product of the angular velocity vector and the lateral velocity vector.

$$\vec{F}_C = 2m\vec{\Omega} \times \vec{v} \tag{2.17}$$

A lateral motion is ensured by suspending the weight on springs, driving an oscillation perpendicular to the vibratory motion, which can be seen in the picture of a typical mechanics model for a MEMS gyroscope in figure 2.1. H. Din describes the mechanical design of a vibratory gyroscope in [22]. For a single axis, the lateral velocity of driven springs can be inserted into the previous equation, resulting in equation (2.18).

$$F_y = -2m\Omega_z A_x \hat{\omega}_x \sin \hat{\omega}_x t \tag{2.18}$$

1 `https://invensense.tdk.com/download-pdf/iam-20380-datasheet/` (viewed last on 26.12.2022)
2 `https://www.st.com/en/mems-and-sensors/a3g4250d.html` (viewed last on 26.12.2022)

F_y represents the Coriolis force in the y-direction, m and Ω are still the proof mass and the angular velocity wanted to measure, respectively. A_x denotes the amplitude and $\hat{\omega}_x$ the oscillation frequency of the oscillating springs. The cross-multiplication produces a perpendicular system of three vectors. Hence a rotation around the z-axis creates a force in the y-direction. Note that the angular velocity is denoted by a capital Ω to prevent confusion with the oscillation frequency. A capacitive pickoff then detects this vibration. After amplifying the changing capacity, filtering and demodulating the signal, a voltage proportional to the rotation rate results. An Analog-to-Digital Converter (ADC) digitizes this voltage.

For the IAM-20380[1], the output is scalable from ± 250 dps to ± 2000 dps and measurement rates from 3.9 Hz to 8 kHz are possible. Excellent noise characteristics with a rate noise density of up to 0.01 dps/$\sqrt{\text{Hz}}$ make it stand out. In contrast, the cross-axis sensitivity of $\pm 5\%$ demands calibration as explained later in section 2.5.
With a range of ± 245 dps and update rates of 100 Hz to 800 Hz, the A3G4250 sensor[2] possesses similar specifications. Unfortunately, it is noisier with a rate noise density of 0.03 dps/$\sqrt{\text{Hz}}$ to 0.15 dps/$\sqrt{\text{Hz}}$. Since in the project, primarily angular rates of ± 1 dps will be present, the sensors have more extensive ranges than necessary. Still, they are currently one of the only available options due to chip shortages and the particular required specifications.

2.4.2. Magnetic Field Sensor

There are two main groups of magnetic field sensors, sometimes also called magnetometers. The first class measures the absolute field magnitude, giving little information about the field's orientation. With instruments of the other category, vector measurements are possible and enable the understanding of the field's direction and, thus, attitude determination. Note that, as explained before in section 2.3, the sensors typically measure the magnetic flux density in the unit T but are often described to measure the magnetic field strength.

While different sensor technologies like fluxgate, magneto-resistive, resonance or hall-effect sensors exist and can be read about in chapter four of [23], this thesis will focus on Magneto-Inductive (MI) sensors. The sensor implemented is an RM3100 by PNI[3] and makes use of their MI technology explained in their White Paper [24]. The primary sensing circuit is shown in figure 2.2a. Here, an external magnetic field H_E can be seen parallel to the magneto-inductive sensor coils and the Schmitt Trigger. An oscillation is created by the Schmitt Trigger changing the output's logical state when the voltage at A increases to a certain threshold. This oscillation forms a waveform voltage at point A. The Current I mimics the voltage waveform and flows over the bias resistance R_b. Since the inductance depends on the physical parameters of the sensor, a constant scales the magnetic field induced by the circuit's current.

$$H = k_0 I + H_E \tag{2.19}$$

This can be seen in equation (2.19), where H is the total magnetic field strength, k_0 is said constant, I said current and H_E is the external field strength wanted to measure. The inductance μ is also a function of the total magnetic field strength H. Therefore, the values of R_B and $U_{threshold}$ are selected carefully to represent the non-linear regime of the permeability curve. An external magnetic field then shifts the regime of the inductance, which in turn increases or decreases the oscillation frequency of the voltage at point A. This shift can be observed in

3 `https://www.pnicorp.com/rm3100/` (viewed last on 26.12.2022)

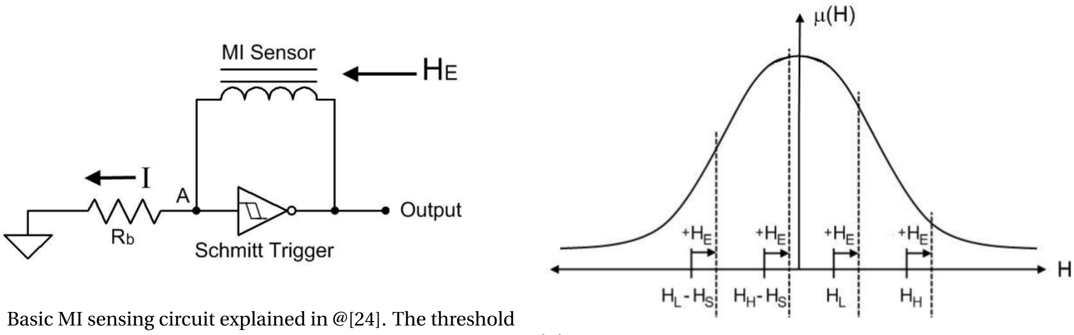

(a) Basic MI sensing circuit explained in @[24]. The threshold voltage for the Schmitt Trigger and the resistance R_b are chosen to represent the non-linear regime of the permeability curve.

(b) The figure shows the shift in the permeability curve from the external magnetic field and is taken from @[24].

Figure 2.2.: The figures explain the principles of the magneto-inductive sensing technology. An oscillation results from the Schmitt Trigger. The external magnetic field H_E changes the oscillation frequency, enabling the determination of the field strength.

figure 2.2b. By measuring the voltage over time, the intensity of the external magnetic field can be determined.

Useful attributes like an inherently digital output, high resolutions of up to 10 nT, low power consumption, no need to (re-)set the sensor, stable output and no hysteresis set the technology apart from, for example, Magneto-Resistive (MR) sensors that are similar in size [24]. Although these characteristics also provide a reasonable basis for usage in space missions where special conditions have to be taken into account, the sensor is not specifically space-grade.

2.5. Calibration

Calibration can have different meanings in different contexts. As Riwanto said in [25], "[It] is a process to produce the best accuracy possible from an instrument by comparing the measurements of the instrument against a reference value and formulating a model which will fit those measurements into the reference value." In a space environment, calibration of sensors may prove challenging as equipment for reference values is rare. Thus, different approaches have to be distinguished.

Preflight calibration benefits from a controlled lab environment and is generally better equipped to perform the procedure. It cannot account for deviations in the sensor performance during the mission, and heavy vibrations during launch may also cause a permanent aberration from the previous calibration. Therefore, an *on-orbit calibration* routine should be developed to ensure accurate sensor readings. A precise reference value must be determined, and physical access to the sensor is impossible. A third option would be *real-time calibration* with estimation filters such as a Kalman Filter [26]. Algorithms used in calibration can also be classified as *recursive estimation algorithm* or *batch estimation algorithm*. In these terms, real-time calibration is considered a recursive estimation algorithm since, with every new information, the algorithm will process the data recursively to gain new knowledge about the sensor. The preflight and on-orbit calibration are usually batch estimation algorithms as they first collect an amount of data and then analyze them to estimate the calibration parameters [25].

In this thesis, only batch algorithms as described later in section 2.5.1 and 2.5.2 are used. The calibration procedures are developed for on-orbit use, but the first tests have been conducted in a lab environment and will be discussed in chapter 4. Therefore, calibration is necessary to eradicate errors from imprecise production, inaccurate mounting, placement close to disturbing (electrical) components and others. These can source different forms of erroneous measurements.

$$\hat{\vec{x}} = \boldsymbol{A}_{no}\boldsymbol{A}_m\boldsymbol{A}_s \cdot \vec{x} + \vec{x}_{off} + \vec{v} \tag{2.20}$$

Equation (2.20) shows how different disturbances influence the measurement $\hat{\vec{x}}$ of the true value $\vec{x}$. Assuming a three-dimensional measurement, $\vec{x}$ gets multiplied with three matrices with dimensions 3×3. The three matrices depicted here represent multiple reasons for corrupt data and may, in literature, be constituted differently like in [27]. In this case, $\boldsymbol{A}_{no}$ is a skew-symmetric matrix representing a non-orthogonality error like high cross-axis sensibility that primarily originates in faulty or imprecise sensor design and production [28]. Mounting of the sensor can also cause non-orthogonality and cross-coupling that is mathematically expressed by the skew-symmetric matrix $\boldsymbol{A}_m$. $\boldsymbol{A}_s$ is a diagonal scale matrix necessary to compensate for production errors. An offset $\vec{x}_{off}$ can arise from DC-currents near the sensor or due to other causes and is therefore added to the rest. $\vec{v}$ is the sensor noise that also corrupts the data, but due to its random nature, it cannot be accounted for in calibration. It is typically assumed to be zero-mean Gaussian white noise and, therefore, should not impact the information in the readings. However, noise limits the sensor's resolution and adds uncertainty to the measurements, impairing the calibration quality. Via oversampling, the influence of noise can be diminished. This technique takes a set of measurements and calculates the mean value so that noisy values cancel each other out. Some sensors have an oversampling factor already implemented, which essentially reduces the data output rate by the factor. Thus, slower measurements should, in theory, always yield the least noisy results.

When calibrating a sensor, the different sources of errors cannot be differentiated. Still, they must be taken into account in a mathematically meaningful way, resulting in equation (2.21).

$$\tilde{\vec{x}} = [\boldsymbol{A}_{no}\boldsymbol{A}_s\boldsymbol{A}_m]^{-1} \cdot \hat{\vec{x}} - \vec{x}_{off} = \boldsymbol{C}\hat{\vec{x}} + \vec{b} \tag{2.21}$$

In this equation, it gets clear that the inverse of the matrix multiplication of the different error sources can only be modeled as one matrix $\boldsymbol{C}$ that serves as the inverse of the product of the error matrices. Subtracting the offset $\vec{x}_{off}$ as well, the calibrated value $\tilde{\vec{x}}$ is achieved. If all parameters could be determined perfectly and no noise would exist, $\tilde{\vec{x}}$ would equal the true value $\vec{x}$, but calibration parameters are always only approximations. For a sensor with three values, for example, a gyroscope sensor measuring the angular velocity of each axis, calibration parameters would consist of a 3×3 matrix and 3×1 bias vector, totaling twelve calibration parameters that have to be determined.

Some types of sensors also have individual error sources due to the property they measure or how the sensor works. For sensors measuring the magnetic field, these error sources are called *hard-iron* and *soft-iron* errors.

$$\hat{\vec{B}} = \boldsymbol{A}_{no}\boldsymbol{A}_m\boldsymbol{A}_s\boldsymbol{A}_{SI} \cdot \vec{B} + \vec{B}_{off} + \vec{B}_{HI} + \vec{v} \tag{2.22}$$

Equation (2.22) looks similar to equation (2.20) but is covers the magnetic field $\vec{B}$. $\boldsymbol{A}_{SI}$ is a full 3×3 matrix modeling the soft-iron error, whereas the hard-iron error $\vec{B}_{HI}$ is an additional offset vector. As their names suggest, these additional errors stem from iron-related materials due to their inherent ferromagnetic properties. Hard-iron errors are permanent magnetic fields close to the sensor that offset the measurement. They can arise from electric currents or magnetized materials. Ferromagnetic materials can get induced by external magnetic fields and therefore strengthen or weaken the measured magnitude in a specific direction, distorting the measurements in a way that can be accounted for with a matrix. One of the chosen calibration algorithms for the magnetometer utilizes this distortion and will be explained in section 2.5.2.

2.5.1. Least Squares Method

Typical calibration procedures focus on simply comparing measured values to a given reference. Due to its well-studied geometric nature and simple mathematical formulation, the *Least Squares Method* (LSM) "is probably the most popular technique in statistics"[29]. Other minimization algorithms, like the *minimization of maximum inconsistency* or the *minimization of the sum of absolute inconsistencies*, are related to weaker statistical concepts, cannot be applied to non-linear problems and are not used as widely as the LSM [30].

The geometric basis of this method can be seen in the example of linear regression in [29]. Calculating the difference between a point $\hat{\vec{x}}$ and a reference point $\vec{x}$ describes the distance between those points. When trying to find the best linear fit to a population of points, the closest line to all points has to be determined. Thus, an error function can be constructed, minimizing the distance.

$$E = \sum_i (X_i - \hat{X}_i)^2 \tag{2.23}$$

Equation (2.23) shows the error value E being calculated by subtracting the i-th measured value $\hat{X}_i$ from the i-th reference value X_i. The resulting difference is then squared and summed over all the measurements taken. In the case of sensor calibration, X_i is a set of three-dimensional vectors containing measurements for three axes, and there are two useful options for formulating the multidimensional error function.

$$E_{standard} = \sum_i (|\vec{x}_i - \hat{\vec{x}}_i|)^2 \tag{2.24}$$

In equation (2.24), the first option is depicted. Here, $E_{standard}$ is the scalar error value resulting from summing the squared norm of the difference of the vectors, where $\vec{x}_i$ and $\hat{\vec{x}}_i$ denote the i-th reference value and measured value, respectively. This case requires excellent knowledge of the reference value as each axis is compared to its corresponding axis. It is considered the standard error function for least squares algorithms.

$$E_{norm} = \sum_i (|\vec{x}_i| - |\hat{\vec{x}}_i|)^2 \tag{2.25}$$

Option two, shown in equation (2.25), looks very similar with the same mathematical descriptions. Here, the difference of each vector's norm is calculated and then squared and summed as well. Compared to the first formulation, this option needs less information about the correct attitude as the magnitude is the comparison factor. As explained in section 2.1.2, the orientation does not influence the vector norm. Both options are feasible, but in section 3.2.1 and section 3.2.2, an analysis of both has been conducted to verify which function works best for a specific scenario.

For multiple measurements, equation (2.24) can also be understood as a system of linear equations. Hence, they can be expressed in a general matrix form as follows in equation (2.26).

$$\begin{aligned} \vec{E} &= \boldsymbol{A}\vec{X} - \vec{B} \\ \vec{B} &= \boldsymbol{A}\vec{X} \end{aligned} \tag{2.26}$$

Where $\vec{E}$ is the residual vector of the system of equations. $\boldsymbol{A}$ is the coefficient matrix, $\vec{B}$ is the reference vector and $\vec{X}$ is the measured vector. In the case of perfect measurements without noise, all entries in $\vec{E}$ equal zero. Wells and Krakiwsky in [30] call $\vec{B}$ the constant vector and $\vec{X}$ the unknown vector with also using different letters denoting the variables. The terminology here is chosen according to the MATLAB documentation of least squares functions[4] for easier understanding of the algorithm. $\vec{X}$ can be determined as the inverse of $\boldsymbol{A}$ times $\vec{B}$. In a general case, $\vec{E}$ is nonzero and has to be minimized. For the minimization, $\vec{E}$ is assumed to be zero to make up a solvable set of linear equations.

Algorithms solving systems of linear equations have been studied thoroughly, and [31] proves the ability to determine a least squares solution by performing a modified Gram-Schmidt orthogonalization (see [32] for the complete algorithm) which calculates a QR-decomposition of the system of equations. This method is also used by Matlab for rectangular matrices as required in the case of calibration, where $\boldsymbol{A}$ is a matrix of dimension $N \times 4$. Usage of the original Schmidt orthonormalization process is not recommended due to its instability and unsatisfactory performance [32]. Today, QR-decomposition algorithms based on household reflections [32] or Givens Rotations [33] are widely used for many applications, including least squares methods. Here, the focus will lie on the technique using Givens rotations because Huang has shown in [34] that Householder transformations need more operations in general and are more complex than Givens rotations.

$$\boldsymbol{A} = \boldsymbol{Q}\boldsymbol{R} \tag{2.27}$$

The algorithm of the QR-decomposition separates the rectangular matrix $\boldsymbol{A}$ from equation (2.26) into an orthogonal matrix $\boldsymbol{Q}$ and an upper triangular matrix $\boldsymbol{R}$ as can be seen in equation (2.27). Orthogonality in a matrix sense means that multiplication with its transpose yields the identity matrix as depicted in equation (2.28).

$$\boldsymbol{Q}^T\boldsymbol{Q} = \boldsymbol{Q}^{-1}\boldsymbol{Q} = \boldsymbol{I} \tag{2.28}$$

$\boldsymbol{Q}$ is made up of several Givens rotation matrices $\boldsymbol{Q}_i$, each zeroing one entry of the lower triangular part of the matrix $\boldsymbol{R}$. A Givens matrix is computed as follows in equations 2.29 and 2.30.

$$\boldsymbol{A} = \begin{bmatrix} a_{11} & a_{12} & a_{13} \\ a_{21} & a_{22} & a_{23} \\ a_{31} & a_{32} & a_{33} \end{bmatrix} \qquad \boldsymbol{Q}_1 = \begin{bmatrix} c_1 & s_1 & 0 \\ -s_1 & c_1 & 0 \\ 0 & 0 & 1 \end{bmatrix} \tag{2.29}$$

4 For example `https://de.mathworks.com/help/matlab/ref/lsqminnorm.html` (viewed last on 26.12.2022)

where

$$c_1 = \frac{a_{11}}{\sqrt{a_{11}^2 + a_{21}^2}} = \cos\theta \qquad s_1 = \frac{a_{21}}{\sqrt{a_{11}^2 + a_{21}^2}} = \sin\theta \tag{2.30}$$

With the angle θ being computed in equation (2.31) by using a polar representation of the values and assuming both to be real as explained in [34].

$$\tan\theta = \frac{a_{21}}{a_{11}} \tag{2.31}$$

In the following equation (2.32), the zeroing calculation is shown in a condensed form. The complete matrix multiplication has more impact than just on the values of a_{11} and a_{21}, but they are insignificant considering the calculations.

$$\begin{bmatrix} c_1 a_{11} + s_1 a21 \\ -s_1 a_{11} + c_1 a_{21} \end{bmatrix} = \begin{bmatrix} \frac{a_{11}^2}{\sqrt{a_{11}^2+a_{21}^2}} + \frac{a_{21}^2}{\sqrt{a_{11}^2+a_{21}^2}} \\ \frac{-a_{11}a_{21}}{\sqrt{a_{11}^2+a_{21}^2}} + \frac{a21 a_{12}}{\sqrt{a_{11}^2+a_{21}^2}} \end{bmatrix} = \begin{bmatrix} \sqrt{a_{11}^2 + a_{21}^2} \\ 0 \end{bmatrix} \tag{2.32}$$

Therefore, multiplication of Q_1 and A yields a matrix with a zero-entry as shown in equation (2.33), where the superscript (1) denotes a change of value for the entry due to the rotation.

$$\boldsymbol{Q}_1 \boldsymbol{A} = \begin{bmatrix} \sqrt{a_{11}^2 + a_{21}^2} & a_{12}^{(1)} & a_{13}^{(1)} \\ 0 & a_{22}^{(1)} & a_{23}^{(1)} \\ a_{31} & a_{32} & a_{33} \end{bmatrix} \tag{2.33}$$

Continuing this procedure for the other entries below the diagonal, an upper triangular matrix can be created:

$$\boldsymbol{R} = \begin{bmatrix} r_{11} & r_{12} & r_{13} \\ 0 & r_{22} & r_{23}^{(1)} \\ 0 & 0 & r_{33} \end{bmatrix} = \boldsymbol{Q}_3 \boldsymbol{Q}_2 \boldsymbol{Q}_1 \boldsymbol{A} = \boldsymbol{Q}\boldsymbol{A} \tag{2.34}$$

equation (2.34) shows this matrix R and also displays how multiplication of the single Givens matrices $\boldsymbol{Q}_i$ determines the orthogonal matrix $\boldsymbol{Q} = \boldsymbol{Q}_3 \boldsymbol{Q}_2 \boldsymbol{Q}_1$. Since $\boldsymbol{Q}$ is orthogonal, its transpose is equal to its inverse: $\boldsymbol{Q}^T = \boldsymbol{Q}^{-1}$. Thus, equation (2.35) is valid.

$$\boldsymbol{R}\vec{X} = \boldsymbol{Q}^T \vec{b} = \vec{b}^{(q)} \tag{2.35}$$

With $\boldsymbol{R}$ being triangular, this set of equations is simple to solve in an iterative procedure beginning with the last row since it only has one value for r_{ii}. Superscript q denotes the new constant vector that needs to be solved. Therefore $x_i = \frac{b_i^q}{r_{ii}}$, and recursively, all values of vector $\vec{X}$ can be determined. It should be noted that the square matrix has only been chosen as the most straightforward example, and the actual application consists of a larger rectangular matrix with $N \times 4$ entries. Due to the unique mathematical properties of a square matrix, other algorithms like the LU-decomposition or Cholesky-decomposition are more effective in that case. Extensive explanations of many algorithms can be found in [35].

As mentioned earlier, the matrix size that has to be calculated is $N \times 4$, with N being the number of measurements, the first three columns being the measured value for all three axes, and the fourth column consisting of negative ones. This last column of ones is added to calculate all twelve calibration parameters in one step, which can be explained by rewriting equation (2.21) into equation (2.36):

$$\begin{aligned}
\hat{\hat{\vec{X}}} = \boldsymbol{C}\hat{\vec{X}} - \vec{b} \quad &= \begin{bmatrix} c_{11} & c_{12} & c_{13} \\ c_{21} & c_{22} & c_{23} \\ c_{31} & c_{32} & c_{33} \end{bmatrix} \begin{bmatrix} \hat{x}_1 - b_1 \\ \hat{x}_2 - b_2 \\ \hat{x}_3 - b_3 \end{bmatrix} \\
\hat{\hat{\vec{X}}} = \boldsymbol{C}^* \hat{\vec{X}}^* \quad &= \begin{bmatrix} c_{11} & c_{12} & c_{13} & b_1 \\ c_{21} & c_{22} & c_{23} & b_2 \\ c_{31} & c_{32} & c_{33} & b_3 \end{bmatrix} \begin{bmatrix} \hat{x}_1 \\ \hat{x}_2 \\ \hat{x}_3 \\ -1 \end{bmatrix}
\end{aligned} \tag{2.36}$$

In equation (2.36), $\hat{\hat{\vec{X}}}$ is the vector of calibrated values, $\hat{\vec{X}}$ is the vector containing measurements. $\boldsymbol{C}$ is the 3×3 calibration matrix and $\vec{b}$ is the bias vector, all in accordance with equation (2.21). Then, a larger 4×3 matrix $\boldsymbol{C}^*$ is introduced, containing all twelve calibration parameters. A negative one is added to the measurement vector, creating the new 4×1 vector $\hat{\vec{X}}^*$. This method of solving least squares problems is the standard procedure of Matlab and has also been implemented as C-code to run on the micro-controller.

2.5.2. Ellipsoid Fitting Calibration Method

As explained in equation (2.22), soft-iron errors distort a magnetic field measurement. Plotting data recorded with an uncalibrated sensor that is turning around all of its axes reveals an ellipsoid. A calibrated sensor (or one without errors) would output a sphere with the radius being the magnetic field strength since it would be the same in all directions. Therefore, an algorithm has been developed in [36] that determines the parameters of the ellipsoid and can use them to calibrate the sensor. An ellipsoid can be mathematically expressed as a general conicoid with equation (2.37).

$$\begin{aligned}
F(\vec{v}, \vec{B}) = a(B_x)^2 + b(B_x B_y) + c(B_y)^2 + d(B_x B_z) \\
+ e(ByB_z) + j(B_z)^2 + p(B_x) + q(B_y) + r(B_z) + s = 0
\end{aligned} \tag{2.37}$$

The 10×1 vector $\vec{v} = [a, b, c, d, e, j, p, q, r, s]^T$ contains all the parameters of the ellipsoid while the 3×1 vector $\vec{B}$ represents the magnetic field strength in x-, y- and z-directions. Determining the parameters of vector $\vec{v}$ is achieved via an LSM.

$$\boldsymbol{A} = \begin{bmatrix} a & d & e \\ d & b & j \\ e & j & c \end{bmatrix} \qquad \vec{n} = \begin{bmatrix} p \\ q \\ r \end{bmatrix} \tag{2.38}$$

Setting up the ellipsoid parameters in a skew-symmetric 3×3 matrix and a 3×1 vector as in equation (2.38) prepares the next step in determining calibration parameters.

$$\boldsymbol{C}_B = \frac{\boldsymbol{A}^{\frac{1}{2}}}{\sqrt{\vec{n}' \boldsymbol{A}^{-1} \vec{n} - s}} \tag{2.39}$$

$$\vec{b}_B = -\boldsymbol{A}^{-1} \vec{n} \tag{2.40}$$

The calibration matrix $\boldsymbol{C}_B$ in equation (2.39) is determined by calculating the square root of the matrix $\boldsymbol{A}$ and dividing by a factor made up of the product of the transpose of $\vec{n}$, the inverse of $\boldsymbol{A}$ and $\vec{n}$ minus the constant of the ellipsoid s. Since the square root of a matrix can have complex results, only the real part of the solution is used. Moreover, the calibration scales the measurements to a unit sphere as it is not necessary for attitude determination to know the absolute field strength. The norm of the reference magnetic field vector can either be multiplied with the calibration matrix as a scale factor, or the measurements can be divided by the reference norm, scaling them down to unit sphere magnitude and making it easier to adapt to a changing magnetic field. Equation (2.40) shows the calculation of the bias vector $\vec{b_B}$ being the negative product of the matrix inverse $\boldsymbol{A}^{-1}$ and the vector $\vec{n}$.

Thus, the calibration parameters for a magnetic field sensor can be determined by directly benefiting from the physical properties of magnetic fields. This algorithm will be compared to a norm least squares method in section 4.4.

Chapter 3. Simulation

3.1. Simulink Model

3.1.1. Gyroscope Model

A gyroscope sensor had already been modeled before based on the BMX055 by Bosch and has been adapted to represent the IAM20380 ([1] on page 25). Since the simulations should prove the feasibility of the calibration algorithm, implementing just one gyroscope model was deemed sufficient.

Figure 3.1 shows the gyroscope model in Simulink. Through the input, it receives an angular velocity in unit degrees per second. A second-order transfer function models the springs inside the gyroscope since it is a vibratory MEMS gyroscope as explained in section 2.4.1. Band-limited white noise and a constant bias are added to the signal, and a gain with the inverse of the sensitivity converts the readings from dps into counts. A quantizer and a zero-order hold block are inserted to mimic the discrete digital output of the sensor. Another second-order transfer function models the sensor's integrated low-pass filter, and a saturation block limits the model's output to a signed 16-bit value. A matrix multiplication applies an error matrix to the vector to simulate an uncalibrated sensor. Finally, the value is multiplied by the sensitivity to convert it into dps again.

This model is then duplicated twice to represent all three axes of movements. The contents of the constant error matrix can be set arbitrarily, but focusing on a real scenario, the inverse

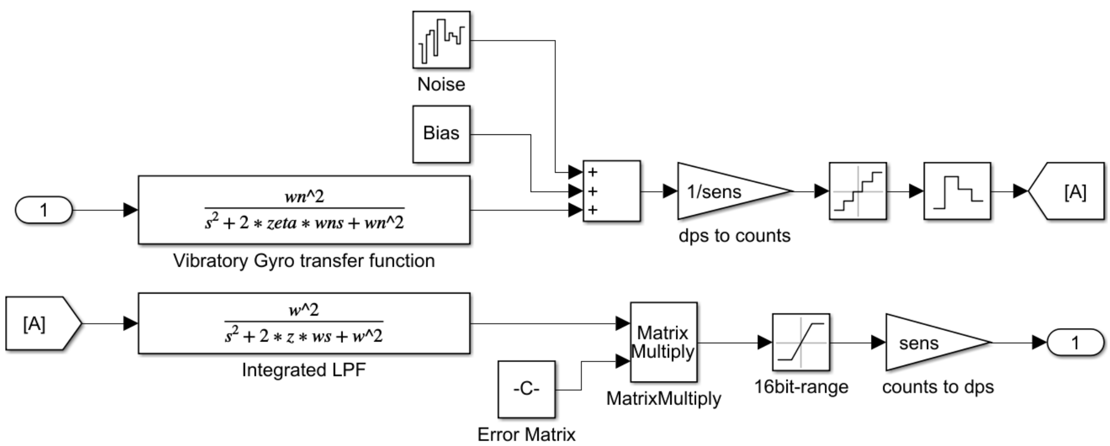

Figure 3.1.: The Simulink model of the vibratory MEMS gyroscope sensor IAM20380 models the springs and integrated low-pass filter with second-order transfer functions. Gain, quantization and zero-order hold blocks discretize the input and errors are integrated for simulating an uncalibrated sensor.

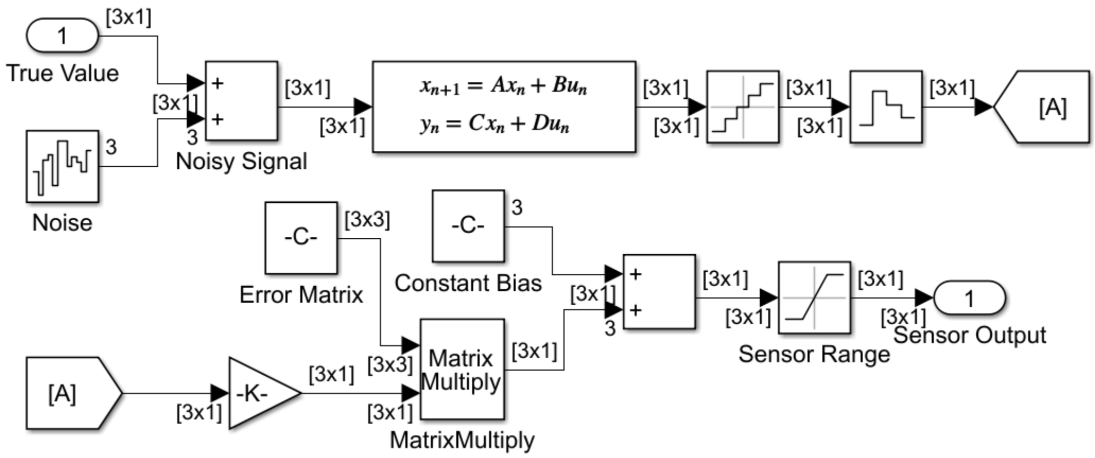

Figure 3.2.: Simulink model of magnetometer RM3100

of the calibration parameters of [8] have been chosen. For comparison, see equation (3.1).

$$C_{gyro} = \begin{bmatrix} -0.979 & 0.060 & -0.008 \\ -0.022 & -1.043 & -0.002 \\ -0.026 & 0.004 & -0.919 \end{bmatrix} \qquad b_{gyro} = \begin{bmatrix} -0.908 \\ 0.794 \\ 0.847 \end{bmatrix} \tag{3.1}$$

Standard deviations of 0.047 dps, 0.048 dps and 0.048 dps for axes x, y and z, respectively, in a simulation without any movement, match the magnitude of the measured standard deviation of 0.057 dps for a similar case as presented later in section 4.2.1.

3.1.2. Magnetometer Model

Modeling of the magnetometer is based on [37] and can be seen in figure 3.2. Since the bias for the calibration should be stable, the integrated random part of the model has been exchanged for a constant block. Also, a quantizer has been introduced to mimic the sensor's sensitivity, and a saturation block keeps the measurements in the range of the sensor. The gain is implemented according to the data sheet ([3] on 26), and the constant block feeding into a matrix multiplication represents the error matrix. Again, the inverse of the parameters in [8] is chosen as the error matrix. Therefore, the calibration should result in the values of equation (3.2).

$$C_{mag} = \begin{bmatrix} 1.140 & -0.066 & -0.041 \\ 0.063 & 1.141 & 0.013 \\ 0.037 & -0.079 & 1.081 \end{bmatrix} \qquad b_{mag} = \begin{bmatrix} -6.161 \\ 4.885 \\ 4.045 \end{bmatrix} \tag{3.2}$$

An analysis of data from the magnetometer model with no movement shows standard deviations of 0.528 µT, 0.456 µT and 0.537 µT for axes x, y and z, respectively. Comparing this to the actual measured standard deviation of 0.424 µT in section 4.2.3 shows a similar magnitude and validity of the model.

Table 3.1.: Errors calculated for calibration parameters gained from standard and norm LSM. The data stems from a simulated full orbit with tumbling rotations up to ±0.08 dps.

Algorithm	$E_{standard}$ / (dps)^2	E_{norm} / (dps)^2
standard LSM	29.86	10.69
norm LSM	508.34	8.23

3.1.3. Others

After modeling the sensors in Simulink, data had to be put in to be *measured* by the simulated sensors. Therefore, a module simulating movements is added. Typical maneuvers are just turning around different axes or imitating the real hexapod's movements from section 4.5. A Low Earth Orbit (LEO) is simulated using orbital parameters in the two-line format. Magnetic field information for a given position in orbit is provided by the implementation of the IGRF model that has been explained in section 2.3.2 or, more specifically, in equation (2.15). Adapting the magnetic field values according to the attitude given by the hexapod model is achieved by calculating rotation matrices which have been explained in section 2.1.2. Thus, the complete setup of satellite movements and sensors has been implemented in Simulink. Data can be plotted live while simulating or analyzed more thoroughly in separate Matlab scripts as they are saved to a file.

3.2. Simulation of Calibration

The calibration parameters of [8] have been inverted and applied to the simulated data as errors to verify the calibration algorithm with a real-world example.

3.2.1. Simulation of Gyroscope Calibration

Different scenarios have been developed to analyze requirements for gyroscope calibration in orbit and the algorithm's robustness. Firstly, the calibration is conducted with data from a typical flight scenario. This means the satellite is slowly tumbling in a range of $\pm 1°$ with an angular velocity of ±0.08 dps in a random matter. Secondly, more significant movements are considered by multiplying all the parameters of the simulated hexapod by 100.

In the first test, the best algorithm had to be determined. Afterward, the robustness of the calibration for different amounts of data was examined. As explained in section 2.5.1, the error function of the least squares method can either sum the difference of each vector norm (denoted here with subscript *norm*) or sum the norm of the vector difference (denoted here with subscript *standard* ord *std*). Next to comparing the resulting calibration parameters to the known error parameters, these functions have also been utilized to quantify the calibration error for verification. Table 3.1 shows the error values for the two different algorithms. As expected, both algorithms perform best in their category of calculation. However, the algorithm taking the norm of each vector first scores a magnitude worse on the other error function, whereas the standard least squares algorithm scores almost as good in the respective other error function. Therefore, the standard algorithm is assumed to deliver better results in the

Table 3.2.: Errors calculated for calibration parameters gained from standard and norm LSM. The data stems from a simulated full orbit with extended tumbling rotations up to ±8 dps.

Algorithm	$E_{standard}$ / $(\mathrm{dps})^2$	E_{norm} / $(\mathrm{dps})^2$
standard LSM	41.05	15.34
norm LSM	7.04×10^6	15.10

calibration. This assumption is supported by reviewing the estimated calibration parameters and a plot of both calibrations.

$$\begin{aligned} C_{standard} &= \begin{bmatrix} -0.816 & 0.044 & 0.002 \\ -0.030 & -0.849 & 0.010 \\ 0.007 & 0.016 & -0.760 \end{bmatrix} \quad & b_{standard} &= \begin{bmatrix} -0.759 \\ 0.623 \\ 0.714 \end{bmatrix} \\ C_{norm} &= \begin{bmatrix} 0.035 & -0.072 & -0.086 \\ -0.008 & 0.740 & -0.042 \\ -0.052 & -0.027 & 0.589 \end{bmatrix} \quad & b_{norm} &= \begin{bmatrix} 0.078 \\ -0.553 \\ -0.597 \end{bmatrix} \end{aligned} \tag{3.3}$$

In equation (3.3), the main disadvantage of the norm LSM is obvious: The diagonal entries should all be negative since the axes' definition is different for the hexapod and the integrated sensor. When just comparing the norm of the measurements, this is not accounted for and will result in significant errors. Also, the first entry is incorrect, with a minimal value. Comparing both matrices to the original matrix, it gets clear that there are large errors, and calibration with just minimal movements does not yield meaningful results. However, the standard algorithm's trend towards the correct solution can be observed as it used the correct signs for the bias.

Hence, for the next test, the velocity and movement range is multiplied by 100 to map a wider variety of motions. This means that with a maximum velocity of 8 dps, a range of angles of ±100° could be achieved. The analysis of this simulation will be exactly as for the normal orbit. The difference between the algorithms gets even more evident in this case as the error values diverge significantly. Verification of the results in table 3.2 can be obtained by comparing the estimated calibration parameters in equation (3.4). Even though the norm LSM determines the values of the main diagonal well, it again fails to differentiate between the signs. Looking at the results of the standard algorithm, the values fit almost perfectly with the actual error parameters, and the deviations are due to noise, which is always the limiting factor in the calibration.

$$\begin{aligned} C_{standard} &= \begin{bmatrix} -0.980 & 0.060 & -0.008 \\ -0.022 & -1.043 & -0.002 \\ -0.026 & 0.005 & -0.920 \end{bmatrix} \quad & b_{standard} &= \begin{bmatrix} -0.908 \\ 0.792 \\ 0.846 \end{bmatrix} \\ C_{norm} &= \begin{bmatrix} 0.980 & -0.045 & 0.036 \\ 0.008 & 1.043 & -0.057 \\ -0.004 & 0.064 & 0.916 \end{bmatrix} \quad & b_{norm} &= \begin{bmatrix} 0.868 \\ -0.750 \\ -0.921 \end{bmatrix} \end{aligned} \tag{3.4}$$

Table 3.3.: Errors calculated for calibration parameters gained from standard and norm LSM. The data stems from a simulated full orbit with extended tumbling rotations up to ±8 dps, but only 300 samples.

Algorithm	$E_{standard}$ / $(\text{dps})^2$	E_{norm} / $(\text{dps})^2$
standard LSM	41.27	15.48
norm LSM	7.04×10^6	15.35

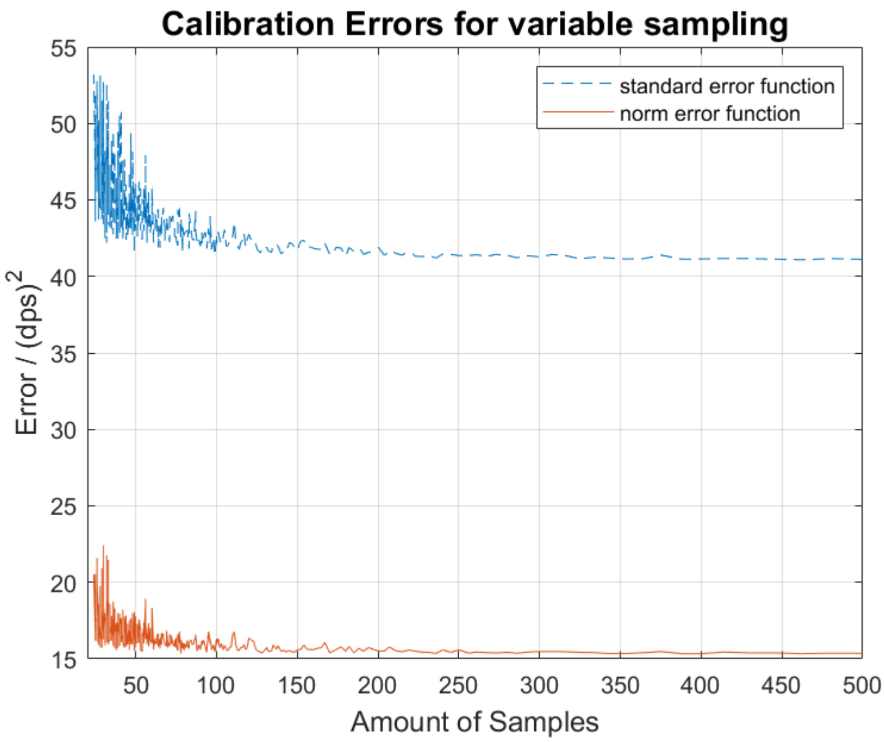

Figure 3.3.: Error of both the norm and standard least squares error functions for the standard LSM algorithm with respect to the data quantity utilized for the calibration.

Scenario two, the magnified orbit tumbling, has been analyzed to understand the amount of data needed to estimate the calibration parameters well. For measurements of five minutes with a 1 Hz update rate equaling 300 samples, the error functions yield the values presented in table 3.3. As one can see, the error very slightly increased. This indicates that a low amount of data can achieve satisfying calibration results. The errors for different data amounts have been computed to investigate this hypothesis further. Figure 3.3 shows how the amount of data changes the error magnitude. The top dashed blue and bottom solid red graphs depict values gained from the standard error function shown in equation (2.24) and the norm error function in equation (2.25), respectively. As it is easy to see, above 150 samples, the errors converge. Below 150 samples, the magnitudes of the errors fluctuate between higher values and similar values to the stable graph above 150 samples. The data quality offers an explanation for this. If, theoretically, the samples all describe the same movement (e.g., a rotation around x with 1 dps), the algorithm is unable to determine different error sources due to too little variation

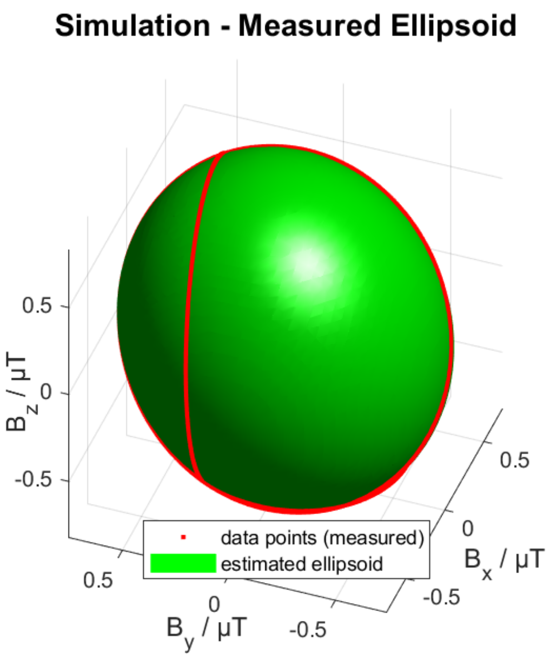

(a) Measured ellipsoid. Radii/μT: a=0.84, b=0.74, c=0.72

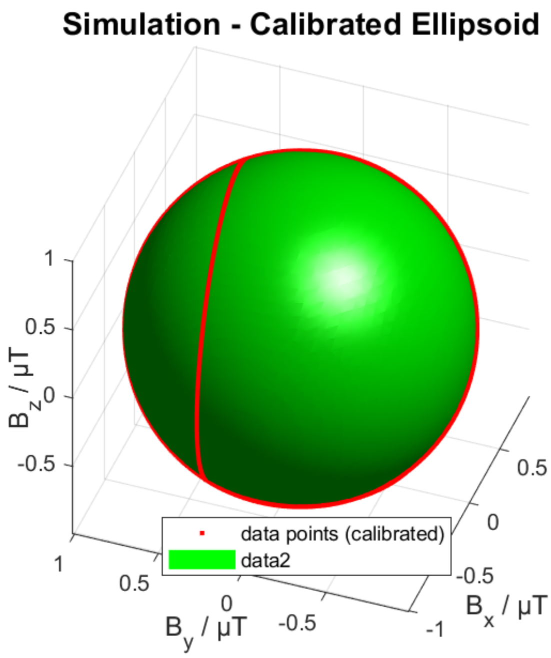

(b) Calibrated ellipsoid. Radii/μT: a=1, b=1, c=1

Figure 3.4.: Ellipsoid calibration with simulated data for rotations without noise. The calibration forces the radii of the distorted ellipsoid into the unit sphere.

in the data. Therefore, low error values can be present even with a few samples of good quality. Still, statistically, the probability of enough variation is higher for larger amounts of data. Moreover, as the plot shows, data above 150 samples, given a case of enough variation in general, promise stability in the quality of the calibration.

Generally, the following findings conclude the simulation of calibration scenarios: The standard least squares method yields the best results calibrating a gyroscope sensor. With more than 150 samples, the quality of the calibration can be assumed to be stagnant. A good data set is given with variation in the movements' magnitude and around each axis.

3.2.2. Simulation of Magnetometer Calibration

Firstly, the ellipsoid calibration has been tested by simulating a complete rotation around each axis in a constant magnetic field without adding noise to the sensor model. This result can be seen in figure 3.4. Figure 3.4a depicts the erroneous ellipsoid while figure 3.4b shows the result of the calibration where the ellipsoid is forced into a perfect unit sphere. The red dots represent the measurements, while the green sphere is the extrapolated ellipsoid.

The same simulations as in section 3.2.1 have also been used to investigate the magnetometer calibration. Also, three calibration algorithms have to be analyzed, with the first two being the same as in the gyro case (standard and norm LSM) and the third algorithm being the ellipsoid calibration. The routines will be verified by reviewing the radii of the estimated ellipsoids and comparing the estimated calibration parameters to the error parameters put

Table 3.4.: Radii calculated for standard LSM, norm LSM and ellipsoid calibration algorithms. The simulated data describes extensive rotations in a constant magnetic field.

Algorithm	$r_1\,/\,(\mu T)^2$	$r_2\,/\,(\mu T)^2$	$r_3\,/\,(\mu T)^2$
Reference	30.478	30.478	30.478
standard LSM	30.498	30.464	30.450
norm LSM	30.464	30.406	30.398
ellipsoid	30.496	30.479	30.460

into the simulation. At first, a constant magnetic field is assumed with hexapod rotations in a range of ±100°.

$$\begin{aligned}
C_{standard} &= \begin{bmatrix} 1.119 & -0.042 & -0.396 \\ 0.063 & 1.134 & -0.005 \\ 0.035 & -0.081 & 1.062 \end{bmatrix} & b_{standard} &= \begin{bmatrix} -6.152 \\ 4.888 \\ 4.047 \end{bmatrix} \\
C_{norm} &= \begin{bmatrix} 1.117 & 0.110 & -0.286 \\ -0.101 & 1.120 & 0.132 \\ -0.070 & -0.176 & 1.091 \end{bmatrix} & b_{norm} &= \begin{bmatrix} -6.156 \\ 4.884 \\ 4.054 \end{bmatrix} \\
C_{ellip} &= \begin{bmatrix} 1.108 & 0.006 & -0.184 \\ 0.006 & 1.139 & -0.033 \\ -0.184 & -0.033 & 1.121 \end{bmatrix} & b_{ellip} &= \begin{bmatrix} -6.160 \\ 4.878 \\ 4.064 \end{bmatrix}
\end{aligned} \tag{3.5}$$

All three calibrations are very similar, as seen in equation (3.5). None achieve to represent the signs of the original error matrix correctly, and considering the diagonal, each algorithm works best for one axis. The same applies to the bias, where each algorithm scores best for one axis, making it difficult to determine the best result. According to the radii in table 3.4, the ellipsoid calibration seems to perform the best, although all results are excellent, and it is impossible to formulate an unequivocal result. This case has been the most interesting considering the later testing since a constant magnetic field is always assumed.

Another simulated calibration is considering a complete orbit in 525 km altitude and large rotations of the satellite in a range of ±100°.

$$\begin{aligned}
C_{standard} &= \begin{bmatrix} 1.120 & -0.046 & -0.393 \\ 0.066 & 1.133 & -0.006 \\ 0.032 & -0.082 & 1.063 \end{bmatrix} & b_{standard} &= \begin{bmatrix} -6.166 \\ 4.879 \\ 4.046 \end{bmatrix} \\
C_{norm} &= \begin{bmatrix} 1.075 & -0.191 & -0.093 \\ 0.237 & 1.112 & -0.244 \\ -0.226 & 0.161 & 1.104 \end{bmatrix} & b_{norm} &= \begin{bmatrix} -6.146 \\ 4.884 \\ 4.059 \end{bmatrix} \\
C_{ellip} &= \begin{bmatrix} 1.101 & -0.002 & -0.169 \\ -0.002 & 1.158 & -0.033 \\ -0.169 & -0.033 & 1.108 \end{bmatrix} & b_{ellip} &= \begin{bmatrix} -6.116 \\ 8.297 \\ 2.623 \end{bmatrix}
\end{aligned} \tag{3.6}$$

Again, no significant difference between the solutions is evident from equation (3.6), and all algorithms perform relatively well. The radii in table 3.5 look similar except for the ellipsoid

Table 3.5.: Radii calculated for standard LSM, norm LSM and ellipsoid calibration algorithms. The simulated data describes extensive rotations during an orbit.

Algorithm	$r_1\,/\,(\mu T)^2$	$r_2\,/\,(\mu T)^2$	$r_3\,/\,(\mu T)^2$
Reference	37.412	36.901	33.968
standard LSM	37.369	36.802	33.937
norm LSM	37.408	36.895	333.957
ellipsoid	38.059	36.337	34.024

calibration. This means this algorithm performs worse than the others for a simulated scenario with much information available for reference.

The following hardware experiments in section 4.4 will focus on more realistic scenarios and determine the robustness of each algorithm. For example, the standard LSM needs accurate information on the current attitude and the sensor's current location. At best, this is only available with a slow update rate and probably less exact as in the simulations. The norm least squares algorithm is a better candidate since it does not need the attitude information, and the magnetic field strength can be assumed to be constant for time frames up to 5 minutes, so a slow update rate is not an issue here. The ellipsoid calibration does not need knowledge of the magnetic field strength if a mapping on the unit sphere suffices for the attitude determination. Another member of the team is currently investigating this.

Chapter 4.

4 Hardware Experiments

In the following, the results of the different tests will be discussed. Starting with a brief description of the used hardware in section 4.1, noise tests conducted on all sensors follow in section 4.2. Next, the calibration of the gyroscopes will be discussed in section 4.3, the calibration of the magnetometer will be addressed in section 4.4, and the verification considering the optical link will end this chapter in section 4.5.

4.1. Hardware and Setup

The terminal was developed at the institute, and the schematics for the sensor integration can be seen in figure 4.1 and figure 4.2.

Figure 4.3 shows the terminal with the important components marked. **RM3100** is the magnetic field sensor ([3] on page 26), **IAM20380** the gyroscope by TDK ([1] on page 25), **A3G4250** the gyroscope by STMicroelectronics ([2] on page 25) and **MSP430** represents the microcontroller by Texas Instruments, specifically the MSP430F5438A[1].

Multiple motorized stages conducted the required motions for testing in different scenarios, each providing advantageous specifications. A collection of the gear used in the first experiments is presented in figure 4.4. The rotation stage LSDH-200WS[2] by Positioniertechnik Meierling executes extensive and fast rotations for all calibration algorithms. While having a maximum speed of up to ±25 dps and a range of up to ±720°, the turntable's motor reaches a resolution of 4.5″ with a repeating accuracy smaller than 18″. Figure 4.4a depicts the rotation stage.

Inclinations on top of the rotation stage can be carried out by the goniometer LSDJ-15HW-02[3] by the same manufacturer. Still fast with a velocity up to ±12 dps, the goniometer's size limits its range to ±15°. A fine resolution of 2.2″ and a repeating accuracy of less than 10″ provide reliable movements. A picture of the motorized goniometer stage can be seen in figure 4.4b. A 3D-printed stand was also used to achieve a 90° attitude of the terminal. The SOLIDWORKS model is depicted in figure 4.4c. Both stages combined have been utilized for the calibration of terminal one and are shown in figure 4.4d.

Smaller motions imitating the satellite's tumbling are accomplished by the Hexapod HXP50-MECA[4] by Newport. Hexapods excel at fine movements with six degrees of freedom. The available product has lateral ranges of ±17 mm, ±15 mm and ±7 mm for x, y and z, respectively with speeds of $\pm 14\,\mathrm{mm\,s^{-1}}$, $\pm 12\,\mathrm{mm\,s^{-1}}$ and $\pm 5\,\mathrm{mm\,s^{-1}}$. Rotations around the x-, y- and z-axis can be performed to ±9°, ±8.5° and ±18° with a maximum speed of ±6 dps, ±6 dps and

1 `https://www.ti.com/product/MSP430F5438A` (viewed last on 30.12.2022)
2 `http://positioniertechnik-meierling.de/produkte/motorisierte-drehtische-serie-lsdh` (viewed last on 30.12.2022)
3 `http://positioniertechnik-meierling.de/produkte/motorisierte-goniometer-serie-lsdj` (viewed last on 30.12.2022)
4 `https://www.newport.com/p/HXP50-MECA` (viewed last on 30.12.2022)

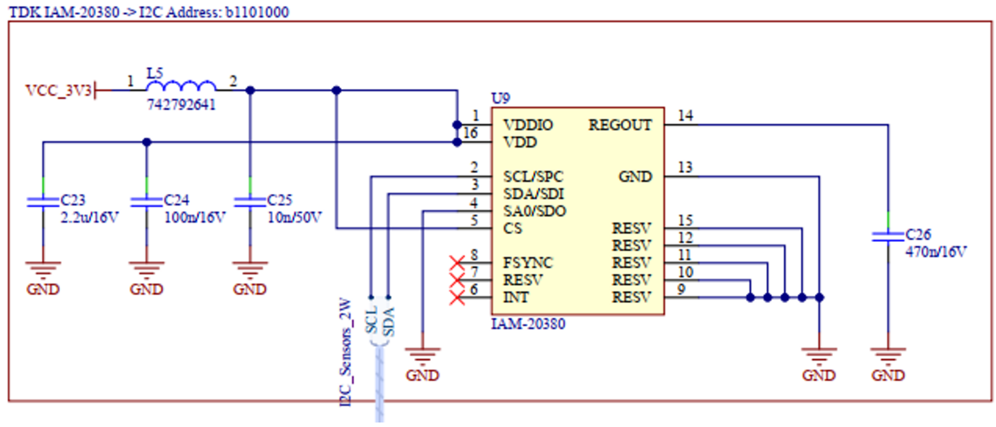

(a) IAM20380

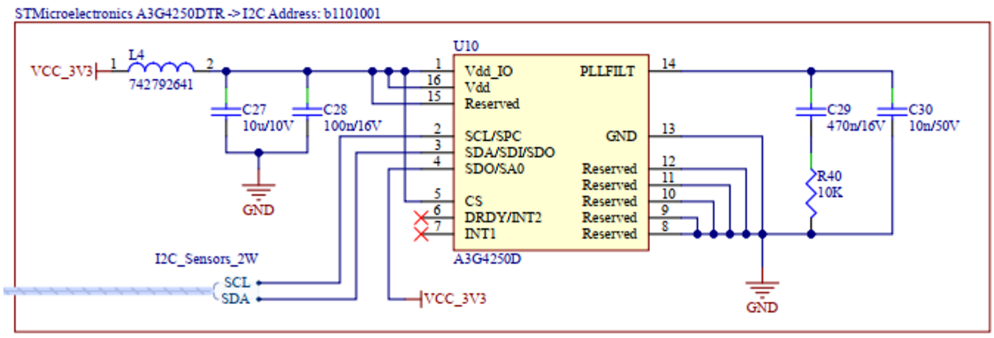

(b) Gyroscope Sensor Schematics A3G4250

Figure 4.1.: Schematics of the implemented gyroscope sensors

±15 dps, respectively. Bi-directional repeatability lies in the magnitude of 0.6 µm for lateral and 0.6 mdeg for rotational movements. The hexapod is depicted in figure 4.5a. Figure 4.5b presents the later setup condensing all available stages into one for full functionality and motion range. The picture shows the gear mentioned above and the final terminal with integrated optics. Note here that the previous picture of the terminal (figure 4.3) presented the terminal's bottom side, as the optics are on top in this implementation. Underneath the Printed Circuit Board (PCB), which is mounted on a breadboard by Thorlabs, the MSP-FET[5] by Texas Instruments can be seen. This is a debug probe for programming and debugging the microcontroller via USB.

A laser aims at the terminal in the final setup to test the optical link. The beam comes from the Optical Ground Support Equipment (OGSE), which imitates an optical ground station (OGS) beacon. Figure 4.6 shows the OGSE in the right half of the picture with the laser originating in the top right corner. It then passes a beam splitter and leaves the OGSE tube slightly to the left of the picture's center. After about 30 cm of free space, the beam hits the terminal's lens. Set to a wavelength of 1590 nm, the laser is also modulated with 10 kHz, which helps differentiate between background lighting and beacon. Equipment for testing also consisted

5 `https://www.ti.com/tool/MSP-FET` (viewed last on 09.01.2023)

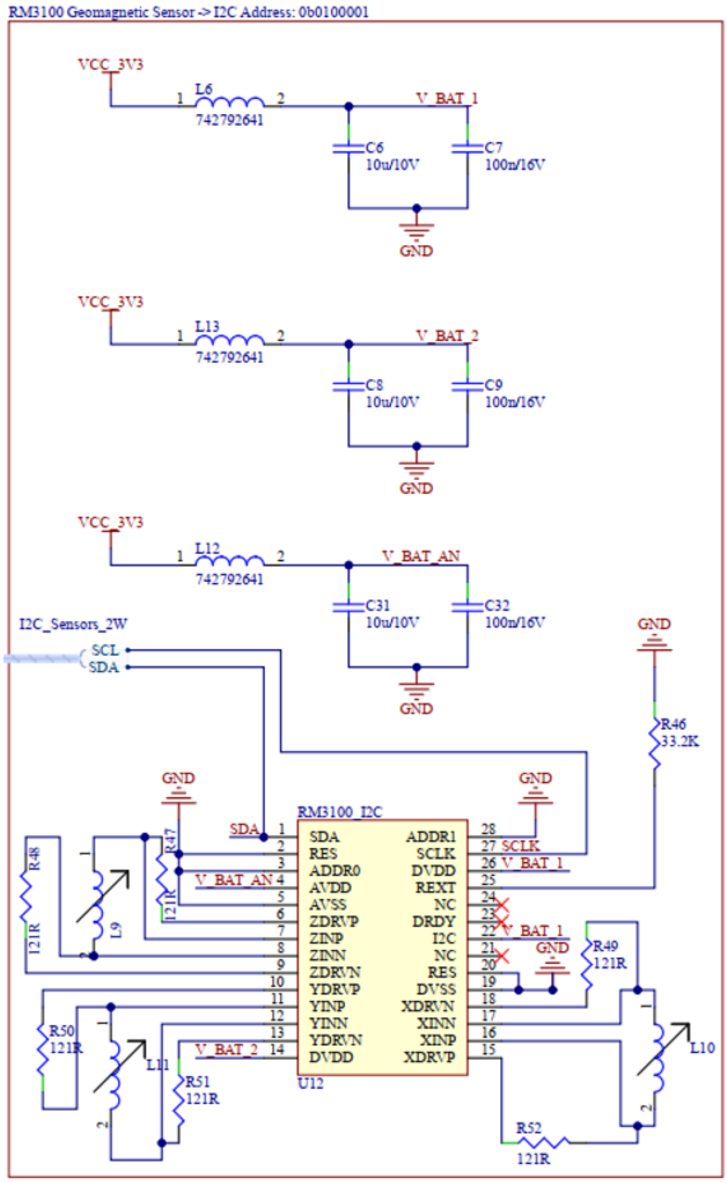

Figure 4.2.: Schematics of the magnetic field sensor RM3100

of a power supply for the terminal and a link to a lab computer for controlling the motors and communicating with the microcontroller.

4.2. Noise Tests

The sensor noise has to be analyzed to gain knowledge on the feasibility of attitude determination with the chosen sensors. According to the datasheet of the sensors, the noise specifications in table 4.1 can be expected. Therefore, the IAM-20380 should yield better results, even accounting for lifetime drift. Regarding the unit, a dependence on the measure-

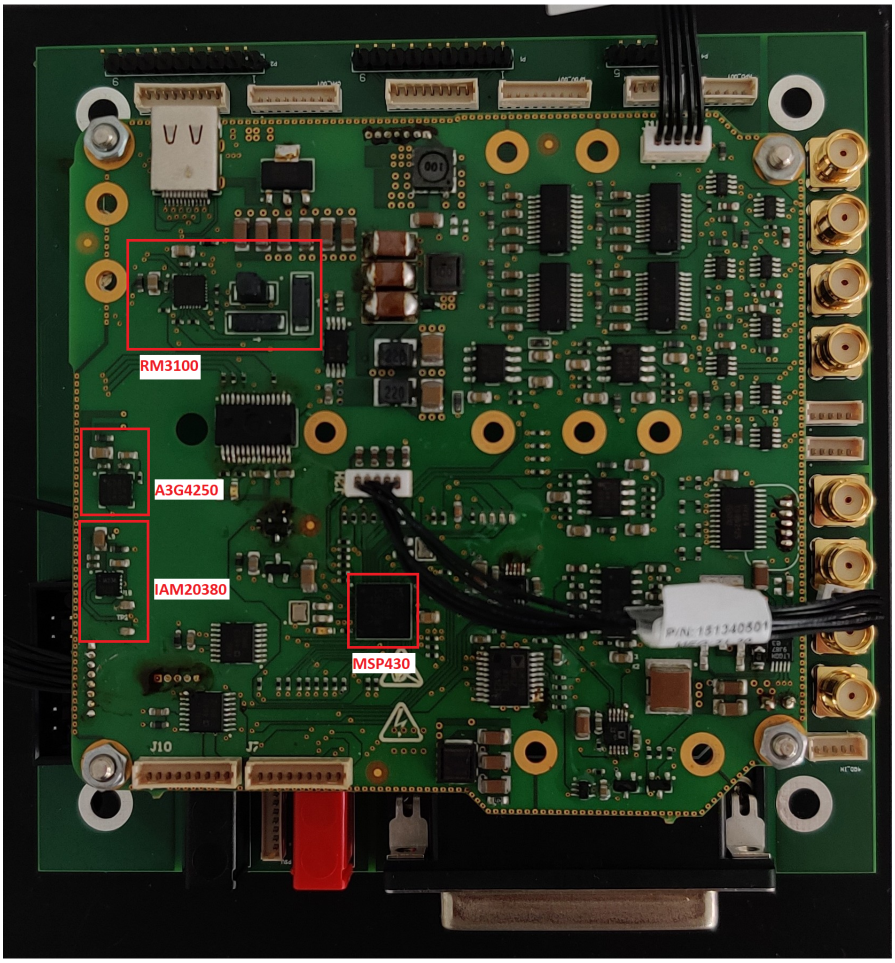

Figure 4.3.: The CubeISL terminal with important components marked.

ment rate becomes obvious; via internal oversampling, for example, slow update rates contain less noise.

Validity of these theoretical values has been investigated by conducting the same test for every possible setting of the sensors. Test conditions consisted of accumulating measurement data for two minutes, with the terminal on a stable platform in a lab environment. After that, two minutes of constant movement have also been conducted to analyze possible differences due to vibrations that the gyroscopes may pick up. Ninety-five tests are needed accounting for every possible sensor setting. Analysis via MATLAB gives insights into the mean value and standard deviation of every data set. According to that analysis, settings that yield the best results have been determined and will be presented in subsections 4.2.1, 4.2.2 and 4.2.3 for each sensor to provide a concise compilation. Afterward, subsection 4.2.4 summarizes the test results, addresses errors and concludes the section.

(a) Rotation stage by Positioniertechnik Meierling[2]

(b) Goniometer by Positioniertechnik Meierling[3]

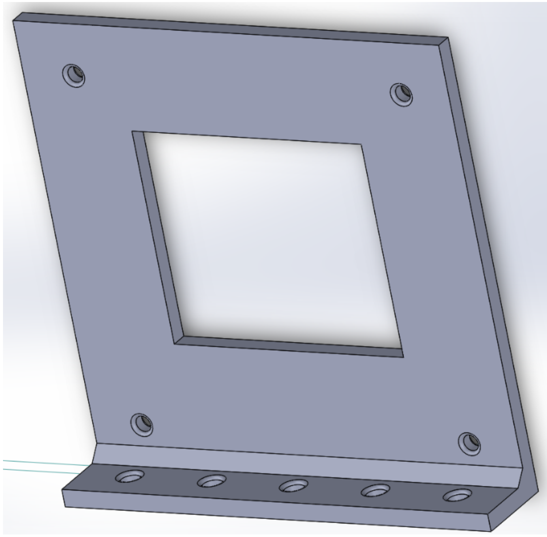

(c) 3D-model of stand

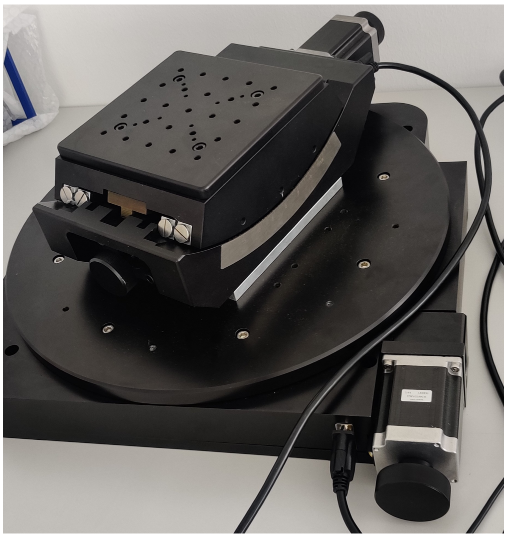

(d) Goniometer and rotation stage combination

Figure 4.4.: Positioning stages used in the lab for the first experiments.

4.2.1. Gyroscope IAM-20380 Noise Test

For the IAM-20380 sensor, a sampling rate of 1000 Hz with an oversampling of five measurements results in an effective update rate of 200 Hz. A lowpass filter with a noise bandwidth of 30.5 Hz and a 3 dB bandwidth of 20 Hz is implemented with the setting as well. This produced a minimal standard deviation of 0.057 dps in the test. Movement on the turntable did not cause considerable deviations from the first results for most settings. This is especially true for the settings with lower lowpass filter values as the IAM-20380 provided the best results by tuning the low-pass filter to a 5 Hz 3 dB bandwidth and a 8 Hz noise bandwidth. At the same time, the output rate was set to 30.3 Hz, equaling an oversampling factor of 33. The lowest standard deviation is calculated as 0.0838 dps and, therefore, slightly higher than in the previous test.

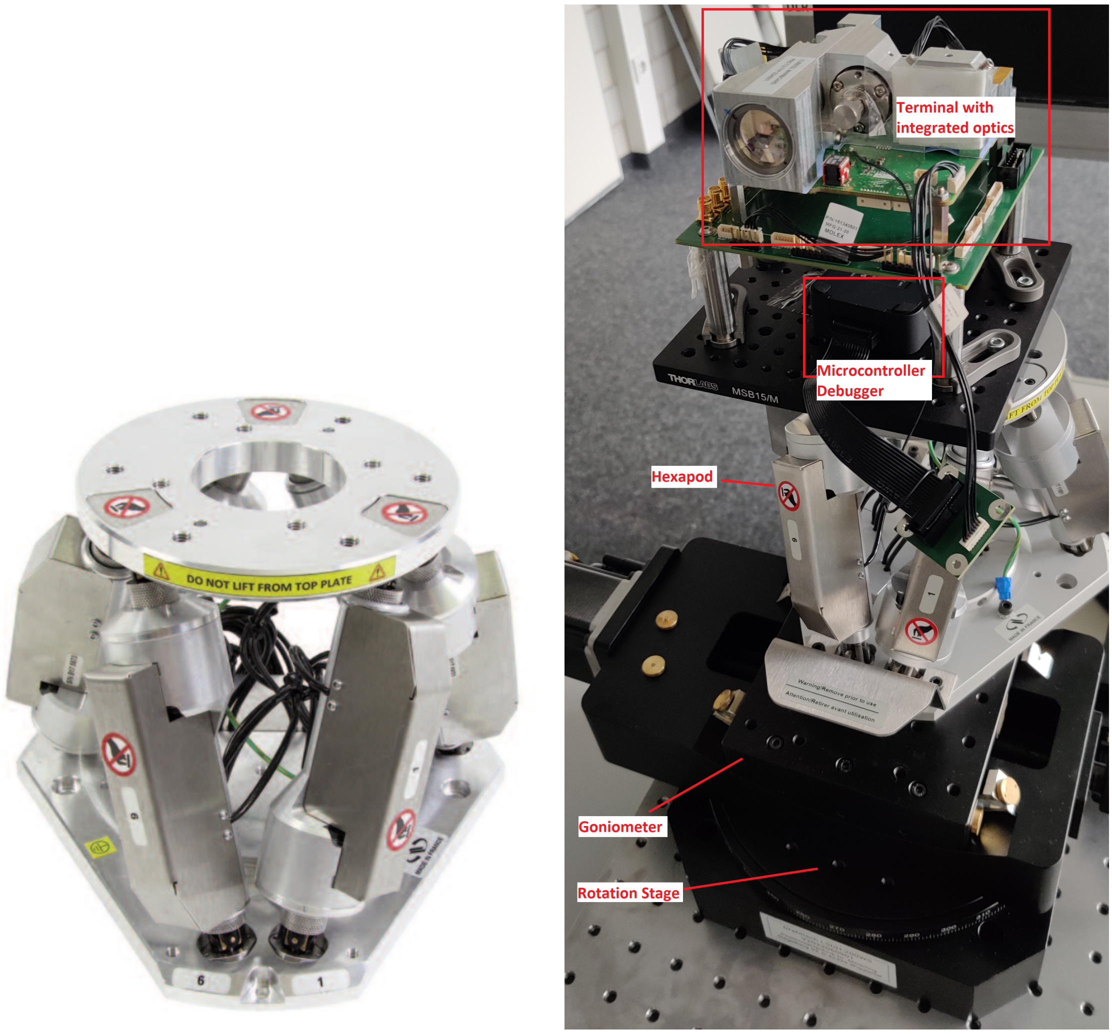

(a) Hexapod HXP50-MECA by Newport[4]

(b) Full calibration setup with important components marked.

Figure 4.5.: The Hexapod is added to the previous setup for a more extensive movement range and the possibility of simulating satellite tumbling.

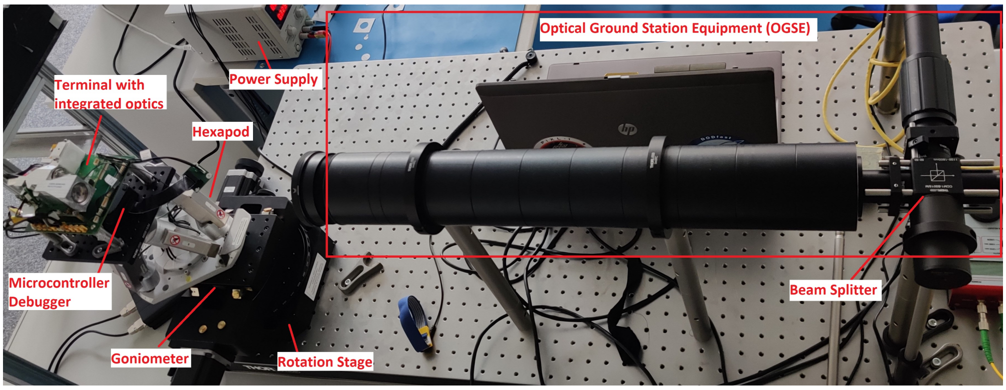

Figure 4.6.: Full testing setup with Optical Ground Support Equipment (OGSE) for link simulation. Important components are marked.

Table 4.1.: Noise Specifications from data sheets([1][2][3] on pages 25 and 26).

Sensor	Noise Specification	Value
IAM20380	Rate Noise Spectral Density	0.005-0.01 dps/$\sqrt{\text{Hz}}$
A3G4250	Rate Noise Density	0.03-0.15 dps/$\sqrt{\text{Hz}}$
RM3100	Noise Density @ Max Single Axis Rate	1.2 nT/$\sqrt{\text{Hz}}$

4.2.2. Gyroscope A3G4250 Noise Test

The second gyroscope, the A3G4250, scored best with a data rate of 200 Hz, a 12.5 Hz cut-off frequency and a highpass-filter with a cut-off frequency of 2 Hz in the stable test. Comparing the minimum standard deviation of 0.2531 dps to the other gyroscope verifies the difference found in the datasheet presented in table 4.1. A similar increase as for the first gyroscope has been noted with the A3G4250 gyroscope in the turning test. It achieved a minimum standard deviation of 0.2653 dps with a measurement rate of 200 Hz, a cut-ff frequency of 12.5 Hz and a high-pass filter setting of 2 Hz.

4.2.3. Magnetometer RM-3100 Noise Test

The lowest standard deviation is determined to be 0.424 µT for the magnetometer with an update rate of 0.3 Hz and the minimal recommended cycle count rate of 30 samples per measurement which essentially describes the oversampling factor. Therefore, the lowest update rate achieves the best results, which is to be expected. Higher update rates perform worse, but still in a valuable regime. Measurements on a turning table with a magnetometer are not meaningful since the values are not constant, and therefore it is impossible to calculate the variance.

4.2.4. Conclusion of Noise Test

Theoretically, all results should look similar to the one of the magnetometer since it yields the best result for the lowest data rate due to more accurate data acquisition. Since this is different with both gyroscopes, the test has to be evaluated very carefully. Offset drifts due to temperature changes, power changes, or other influences can drastically affect the results of sensitive sensors like gyroscopes. Therefore, more extended testing periods and cautiously ensuring the same conditions would be necessary to gain validation of the findings. Nevertheless, the test verified the superiority of the IAM-20380 in terms of noise and helped choose filter options for both gyroscopes. The sensor has very stable noise characteristics and consequently provides valuable measurements even at a 1 kHz measurement rate. Since the fastest output rate is targeted for the project, the perfect setting is not necessarily the one with the least noise.

While the significant noise disqualifies the A3G4250 sensor, its extremely low and stable offset complies with the datasheet's information. This made it a valuable candidate since offsets are the biggest problem with attitude determination with gyroscopes. Hence, a mix of both gyroscopes would prove ideal for the project but is currently unavailable. Evaluation of the noise tests while moving the terminal on a turntable showed no significant performance loss for most settings and helped gain additional insight into the best filter options for actual measurements. Depending on the final utilization of the magnetometer readings, a good compromise between the sampling rate and the accuracy of the measurements has to be found.

4.3. Gyroscope Calibration

As explained in section 2.5, the calibration of a gyroscope needs movements around every axis at different velocities to account for different sources of error. Many experiments have been conducted, each slightly changing the conditions to determine the best results. Furthermore, two identical terminals have been used, and each sensor has to be calibrated to diminish the differences in production and mounting. The results for the two terminals will be discussed in the following. Considering the results of the noise test, the calibration results of the gyroscope IAM20380 will be the focus. Calibration parameters for the A3G4250 will be determined just once in the final application of the algorithm for the sake of completeness.

4.3.1. Terminal 1

Terminal one was primarily used in this work's early phase, as the optics still needed to be implemented. Therefore, the movements for the calibration were only performed on the turntable and goniometer to test the calibration routine. The 3D-printed stand was used to prop up the terminal for 90° to turn around every axis. For the movement set, a wide range of different velocities was chosen with the turntable driving +15, −10, +5, −2.5, +1.25 and finally +10 dps for at least 10 seconds each. This accounts for more than one minute of data per axis.

Figure 4.7 shows the z-axis of the IAM20380 gyroscope sensor on the first terminal. Raw measurements, calibrated sensor data and reference data from the turntable are plotted in dashed blue, dotted red and solid black, respectively. Movements of the dashed blue line indicate non-orthogonalities, and an offset can also be observed. Estimating the calibration parameters yields the results depicted in equation (4.1).

$$C_{t1,iam20380} = \begin{bmatrix} 0.998 & 0.006 & -0.003 \\ 0.002 & -0.996 & 0.014 \\ -0.038 & 0.030 & 0.995 \end{bmatrix} \qquad b_{t1,iam20380} = \begin{bmatrix} -1.329 \\ 0.457 \\ 0.593 \end{bmatrix} \tag{4.1}$$

Calculating the norm of the matrix gives 1.018, and the matrix is very similar to the unit matrix, with the y-axis being inverted. Interestingly, the estimated bias vector is relatively large compared to the second gyroscope. Calibration of the A3G4250 sensor yields similar results as shown in figure 4.8. This plot is built the same way as before, with the dashed blue line representing the raw measurements before calibration, dotted red being the calibrated values, and solid black showing the reference values of the turntable. As seen in the noise test, the bias is much smaller on this gyroscope than on the first sensor, but the noise is much larger. For this excerpt, the movements are still clearly visible as velocities of 5 to 15 dps are depicted. However, the noise would be too large to recognize movements of small velocities around 0.1 dps as is expected on the satellite. Still, the calibration parameters have been determined and are depicted in equation (4.2). Since the second axis also has a negative value here, the

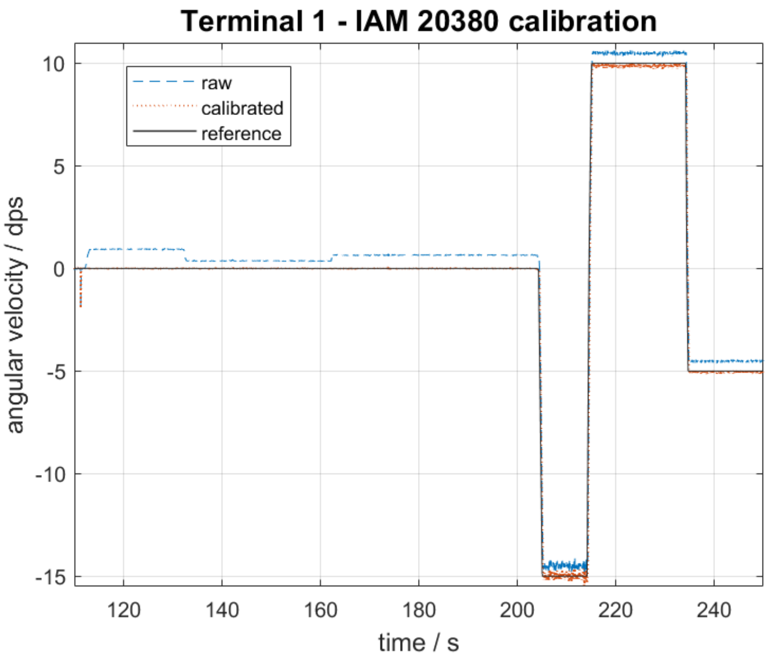

Figure 4.7.: Calibration results for IAM20380 on terminal 1. There are significant cross-axis errors visible in the raw data. The calibration diminishes these effects.

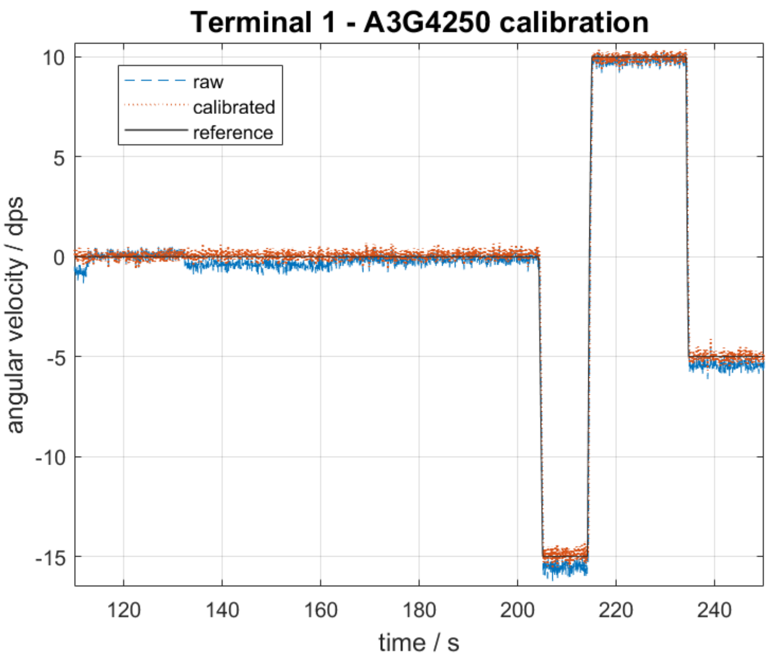

Figure 4.8.: Calibration results for the A3G4250 on terminal 1. The unfavorable noise characteristics can be observed. Diminishing cross-axis effects with the calibration works well.

definitions of the coordinate system of the sensors appear to be the same and comply with the CAD model.

$$C_{t1,a3g4250} = \begin{bmatrix} 0.996 & 0.010 & -0.015 \\ 0.009 & -0.989 & 0.013 \\ -0.035 & 0.025 & 0.981 \end{bmatrix} \qquad b_{t1,a3g4250} = \begin{bmatrix} 0.008 \\ 0.183 \\ -0.313 \end{bmatrix} \tag{4.2}$$

The norm of this calibration matrix is 1.0145. Therefore, it is close to one, and the calibration can be validated visually.

4.3.2. Terminal 2

The second terminal was completed in the laboratory, where the optical components were also tested. For that, the terminal was placed on the turntable, goniometer and hexapod, accounting for a more extensive range of operations. After the calibration, this terminal was also used to simulate a downlink and compare the angular movements of the FSM to the sensor data. With the more extensive range of operations of the laboratory setup, more variable data could be sampled after implementing a function to calculate the rotations for different angles. Since the satellite can only provide slow attitude information with a 1 Hz update rate, various scenarios and amounts of data are analyzed in the following to recognize the feasibility of the routine.

Calibration 1 - All possible data

First, the test with the complete data set will be discussed as it should, in theory, yield the best results. The goniometer has a range of $\pm 15°$ around the x-axis, while the hexapod can provide movements around each axis with up to $\pm 9°$. Together with 90° rotations around the x- and y-axis (φ and θ, respectively) by the 3D-printed stand for the terminal, the angles in table 4.2 were implemented using the goniometer and hexapod. Then, the turntable performed movements at different speeds. Notice here that the z-axis (ψ) was not used since it is the same axis that the turntable moves around. Equation (2.4) is used to determine the true angular velocities by multiplying the rotation matrices with the unit vector of the z-axis shown in equation (4.3)

$$e_z = \begin{bmatrix} 0 & 0 & 1 \end{bmatrix}^T \tag{4.3}$$

Data given by the gyroscopes is then compared to the calculated reference velocities in a least squares matter as explained in section 2.5.1 to determine the calibration parameters yielding the best results. Using the entire data of all 14 positions, the algorithm outputs the calibration matrix and bias vector given in equation (4.4)

$$C_{t2,all} = \begin{bmatrix} 0.982 & 0.014 & 0.024 \\ -0.013 & 0.992 & -0.014 \\ -0.019 & -0.030 & -1.008 \end{bmatrix} \qquad b_{t2,all} = \begin{bmatrix} 0.159 \\ 1.035 \\ -0.252 \end{bmatrix} \tag{4.4}$$

Typically, the calibration matrix is close to the identity matrix, which can also be seen in the first two columns. The third column is negative since the axes' definitions of the hexapod and the sensors differ. The norm of the calibration matrix is 1.022. In figure 4.9, a section of the z-axis of this calibration is depicted. The plot shows the angular velocity in degrees per

Table 4.2.: All available angles used for the calibration of terminal 2.

Data Set	φ / °	θ / °	ψ / °
1	0	0	0
2	-90	0	0
3	90	-90	0
4	-66	0	0
5	-75	-8	0
6	-75	9	0
7	66	-90	0
8	75	-82	0
9	75	-99	0
10	105	-90	0
11	-15	0	0
12	-15	8	0
13	-15	-9	0
14	-24	0	0

second measured by the gyroscope (blue, dashed), the calibrated data (red, dotted) and the previously calculated correct data (yellow, solid), plotted against the time in seconds. The complete data set contains a time interval of 1500 seconds altogether since all of the 14 tests had a duration of a little over 100 seconds. Furthermore, the negative c_{33} value means that the sensor coordinate systems and the reference values are defined opposite to each other on the z-axis. This is explained by the sensor being upside-down. Therefore, the calibration sets the sensor coordinate system to the hexapod coordinate system.

Calibration 2 - only 90 degree rotations

Another result could be achieved by just using the terminal's data on the 3D-printed stand without using the hexapod or goniometer for additional positions. Therefore, the test conditions are the same as in section 4.3.1, except using only the first three data sets of table 4.2. The parameters in equation (4.5) better resemble the identity matrix, while the bias vector is similar to the test with all available data. Interestingly, the norm of the calibration matrix is also 1.022 and, thus, just slightly larger than the unit norm.

$$C_{t2,90deg} = \begin{bmatrix} 0.993 & 0.009 & 0.015 \\ -0.013 & 0.997 & -0.014 \\ -0.035 & -0.037 & -0.995 \end{bmatrix} \qquad b_{t2,90deg} = \begin{bmatrix} 0.137 \\ 1.052 \\ -0.260 \end{bmatrix} \tag{4.5}$$

Visual verification of the calibration can be seen in figure 4.10 where the z-axis is depicted with angular velocity in degrees per second with respect to time in seconds for raw sensor data, calibrated data and reference angular velocity, respectively. Generally, the dotted red plot with the calibrated data follows the solid yellow line of reference values very well. Moreover, focusing on the dashed blue line of raw measurements, some non-orthogonality errors can be seen when there should be no movement. Still, the sensor detects some nonzero values

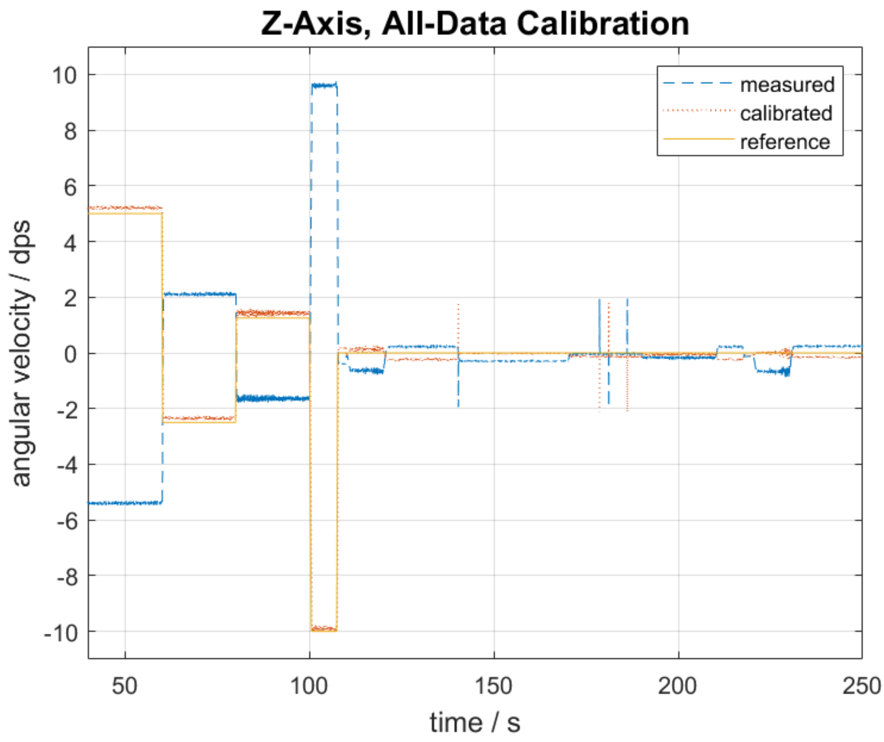

Figure 4.9.: Z-Axis with all data calibration. A remaining cross-axis sensitivity can be observed.

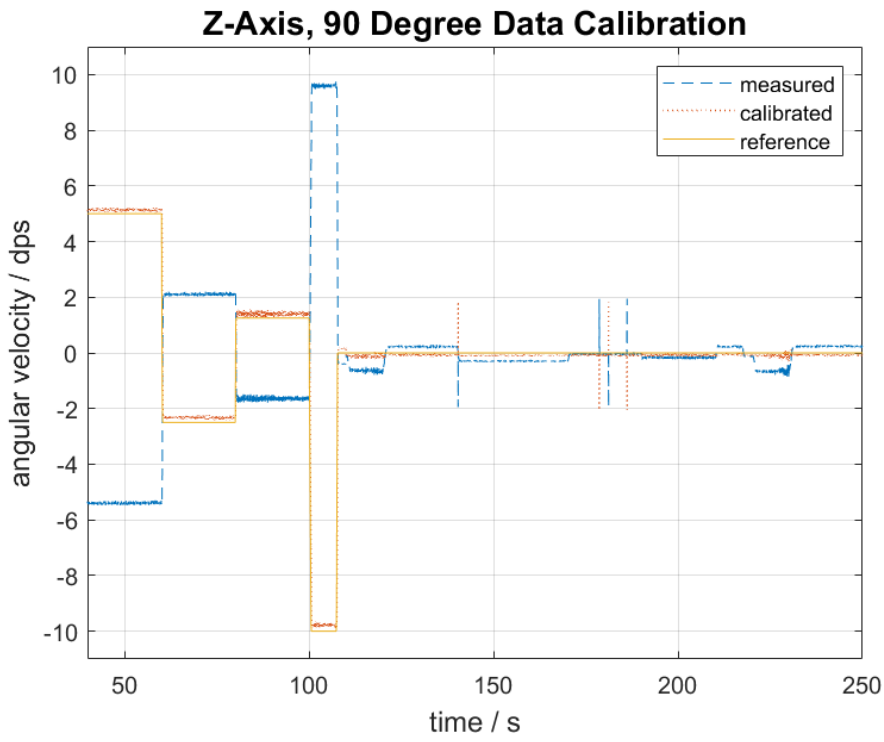

Figure 4.10.: Z-Axis with calibration from three perpendicular data sets. Satisfying results can be observed.

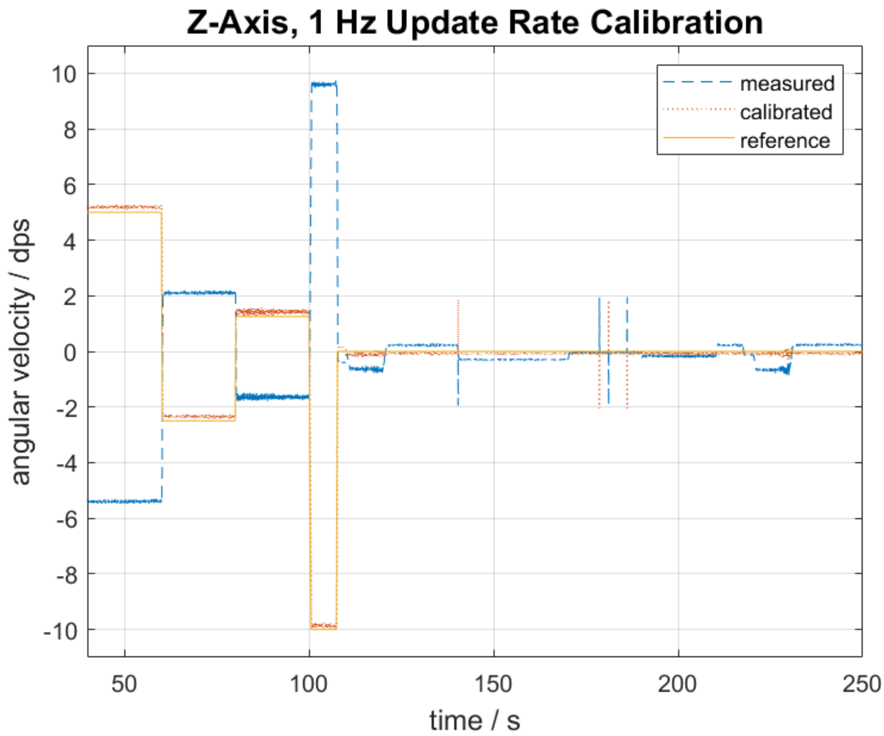

Figure 4.11.: Z-Axis with calibration from only slow update rate of perpendicular data. Satisfying results can be observed.

from other axis' rotations. After the calibration, these erratic values are not visible anymore, contributing to the qualitative verification of the results. Since the matrix represents a unit matrix more and, visually, these calibration parameters are better at diminishing cross-axis effects, just the three orthogonal data sets will be used going forward.

Calibration 3 - 1 Hz Update Rate

The last experiment will test the algorithm's functionality for a real application in space. Therefore, the amount of data used for the calibration is reduced to an update rate of 1 Hz and only the data set of the 90° assembly is used since it yields the better result as shown in section 4.3.2. The calibration parameters are then determined as depicted in equation (4.6).

$$C_{t2,1Hz} = \begin{bmatrix} 1.001 & 0.010 & 0.015 \\ -0.014 & 1.013 & -0.013 \\ -0.035 & -0.037 & -1.003 \end{bmatrix} \qquad b_{t2,1Hz} = \begin{bmatrix} 0.150 \\ 1.074 \\ -0.256 \end{bmatrix} \tag{4.6}$$

Remarkably, the main diagonal values of the matrix are larger than one, which has not been the case before. This does not affect the matrix's norm much, as it is still very close to one with a value of 1.0310. The values next to the diagonal are almost identical to those previously displayed. Considering the bias vector, the first two entries possess the most significant difference compared to the results of equation (4.5). Figure 4.11 shows the same plots, with the

Table 4.3.: Comparison of the calibration errors of terminal 2 with different data sets.

Data	E_x / (dps)^2	E_y / (dps)^2	E_z / (dps)^2	E_{std} / (dps)^2	E_{norm} / (dps)^2
Uncalibrated	164.391	2.906×10^3	4.746×10^5	4.777×10^5	1.099×10^4
All data	70.159	27.482	948.53	1.046×10^3	820.811
90° Data	65.887	26.303	933.348	1.025×10^3	805.896
1 Hz Data	63.569	26.446	939.079	1.029×10^3	811.579

dotted red graph being the calibration with fewer data. This indicates that the calibration with fewer data points performs, visually speaking, equally as well as the calibration with faster data acquisition.

Comparison of Gyro Calibration Results

In this subsection, the results of the previous subsections will be analyzed to gain mathematical and visual insight into how well the calibration algorithm performs under different circumstances. For that, data unrelated to the calibration is put in the error functions (equations 2.23, 2.24 and 2.25). The data set was collected for a different experiment but with the same terminal, so the same calibration parameters should apply. Note that only a rotation around the z-axis was performed in the data set, explaining the high values for E_z. As shown in table 4.3, the calibration with limited data of only perpendicular attitudes yields the best results with minimal error in all categories except for the x-axis, where the 1 Hz calibration scores even better. Generally, the all data calibration yields inferior results, and the 90° data is the best, with the 1 Hz set only slightly behind. The differences between the calibrations are minimal when comparing the computed errors to the uncalibrated sensor data.

Figure 4.12 shows two different, more zoomed-in excerpts of the data set used for the calibration. Each picture displays all three calibrations and the reference data. The dashed blue graph in each depicts the all-data calibration, while the dotted red line and the dash-dotted yellow line represent the same 90° data sets with different amounts of samples utilized for calibration. Lastly, the solid violet graph indicates the reference value. Comparing them shows no significant difference while moving. When the reference value is zero, a slight movement can be seen in the all-data calibration plot, whereas the other two plots are stagnant with just a small offset to the true line. This would suggest that the first calibration is not as good at annihilating cross-axis effects as the others.

Different aspects have to be examined when considering this information. Theoretically, more data should account for better calibration results, but as shown in figure 3.3, saturation is reached with a certain amount of valuable data. Thus, the quality of the regarded data is more influential on the result than the number of samples. Also, the offset is responsible for most of the differences between reference and measured data, so the mathematical interpretation mostly gives an impression of how well the bias is determined. Systematic problems of the experiment have to be taken into account. Firstly, the mounting of the terminal on the 3D-printed stand is relatively loose, and a perfect 90° cannot be ensured. Similarly, the hexapod and goniometer, though much more precise, cannot guarantee a perfect attitude. Secondly, mechanical inaccuracies and looseness of the turntable are possible error sources. Every manual intervention to the test setup increases the uncertainty about the mounting

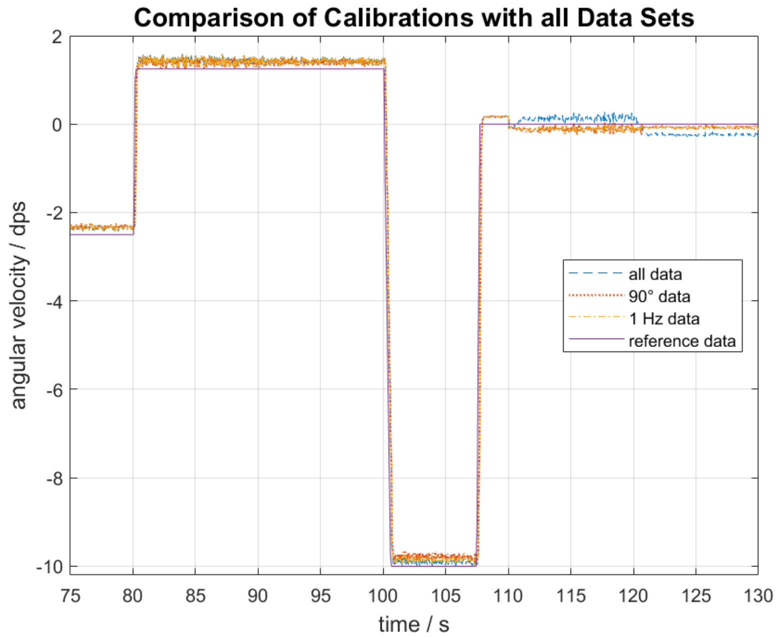

(a) Z-Axis: Comparison of all calibrations

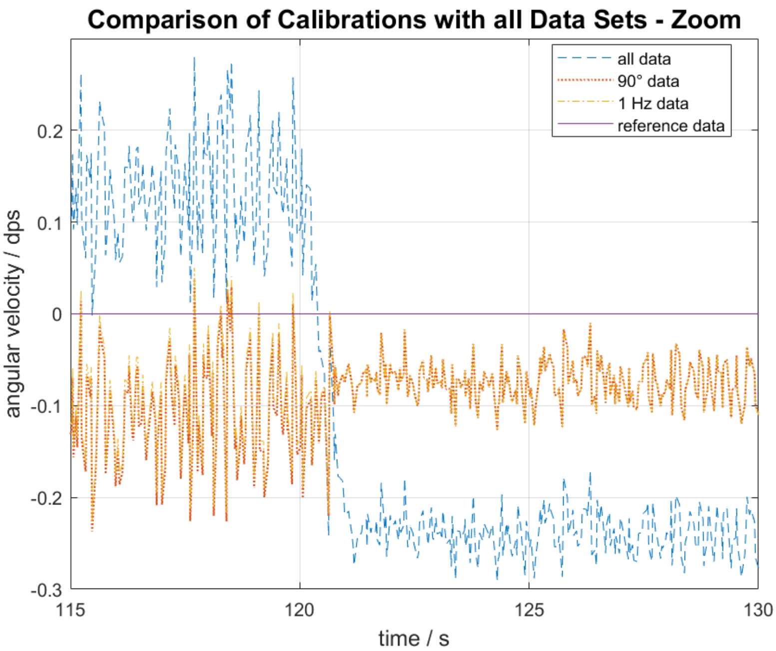

(b) Z-Axis: Comparison of all calibrations - zoomed in

Figure 4.12.: Comparison of Z-axis of all calibrations in different zooms

error. Hence, more data sets also yield a significantly higher chance of considerable flaws. At last, noise and bad data are other limiting factors to the success of a calibration. For this, one might notice the spikes in figure 4.12. Those spikes most likely originate from electrical spikes in the sensor and must be classified as bad data points outside normal noise. Detecting and filtering such bad data points is essential in ensuring useful calibration results.

Therefore, these results have to be viewed cautiously, but the main finding is that the calibration with relatively little data works almost as well as with more data. This also matches the simulation results of section 3.2.1. In the mission scenario, the error sources of the lab setup cease, as the sensors are permanently fixed after launch, and an on-orbit calibration is intended.

4.4. Magnetometer Calibration

Calibration of the magnetometer as explained in section 2.5.2 proved to work efficiently in simulations as shown in section 3.2.2. Special equipment is necessary to conduct tests in a clean magnetic environment. As this equipment has not been available, many measurements have been heavily affected by magnetic disturbances. An example of the resulting distortions can be seen in figure 4.14a with the red dots depicting the measured data points and the green area showing the estimated ellipsoid. The varying magnetic field strength may stem from electric currents in the laboratory's equipment and surrounding magnetic materials. The proximity to the motors of the goniometer and rotation stage might also affect the measurements.

Therefore, a few measurement series have been conducted outside in a cleaner environment. To ensure as little disturbances as possible, the data was collected on the football field of the DLR with few surrounding buildings, which can be seen in figure 4.13. Thus, reference data from the IGRF model was also available. Only terminal 2 has been taken outside for the measurements. Therefore, all findings in this section characterize terminal 2. A depiction of the ellipsoid calculated from the raw measurements outside can be seen in Figure 4.14b. The red dots again represent the measured points, while the green conicoid is the estimated ellipsoid, showing the error's influences. Since terminal 2 has been used for both measurements of figure 4.14, the sensor errors should be similar. The laboratory distortions are substantial compared to the measurements in a cleaner environment. Thus, the calibration is only conducted on clean data.

$$
\begin{aligned}
C_{norm} &= \begin{bmatrix} 0.992 & -0.043 & 0.468 \\ -0.077 & 1.019 & -0.350 \\ -0.446 & -0.319 & 0.986 \end{bmatrix} \qquad & b_{norm} &= \begin{bmatrix} -13.438 \\ -14.282 \\ -12.415 \end{bmatrix} \\
C_{ellip} &= \begin{bmatrix} 1.090 & 0.010 & -0.0013 \\ 0.010 & 1.069 & -0.010 \\ -0.001 & -0.010 & 1.146 \end{bmatrix} \qquad & b_{ellip} &= \begin{bmatrix} -5.530 \\ -8.327 \\ -17.783 \end{bmatrix}
\end{aligned}
\tag{4.7}
$$

Equation (4.7) shows the calibration parameters for the outside data while table 4.4 displays the radii. A relatively large divide between both algorithms becomes obvious in the calibration parameters. Since the norm of the measurements is smaller than the expected magnetic field strength, both algorithms compensate for that. Therefore the norm of both matrices is slightly larger than 1 with a value of around 1.147 for both algorithms.

As it is easy to see, the ellipsoid calibration fits the radii better to the true magnetic field

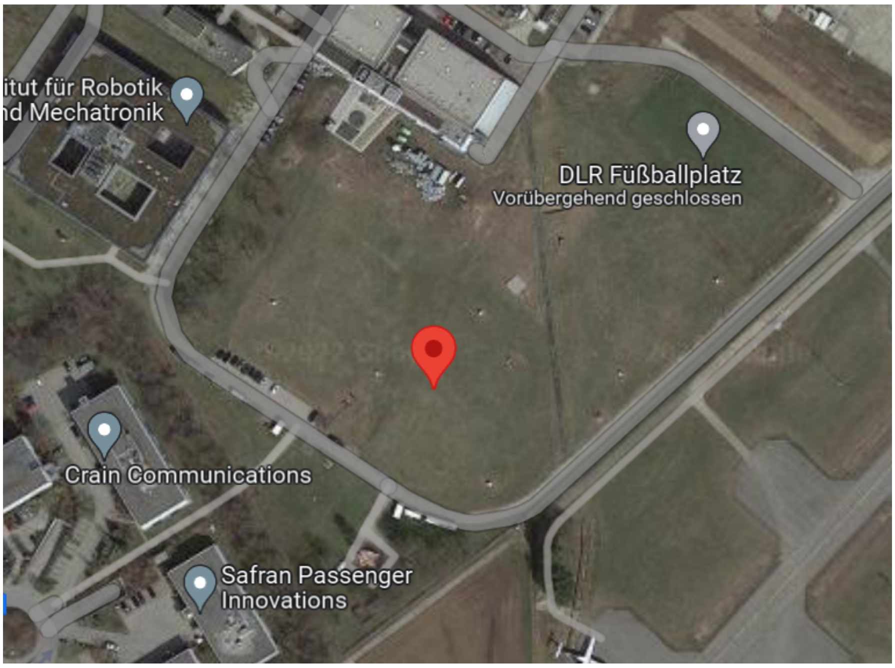

Figure 4.13.: Location of magnetic field measurements. @`https://www.google.com/maps` Coordinates: 48°4′57″ N, 11°16′37″ E

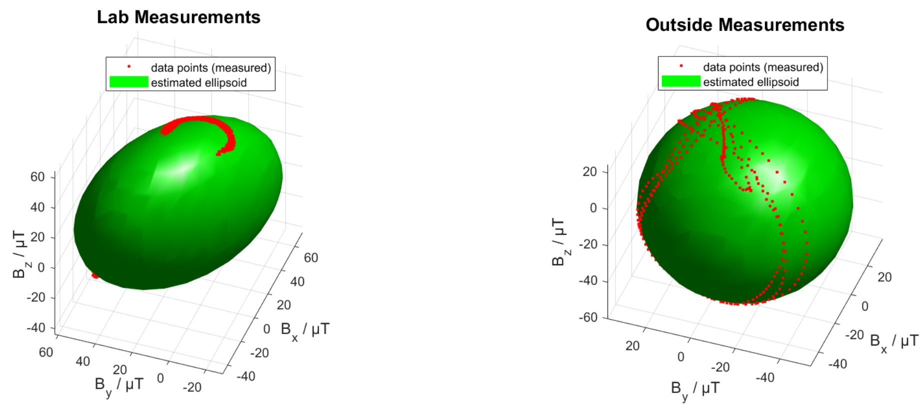

(a) Ellipsoid from Raw Lab Measurements. Radii/µT: 65.27, 54.25, 36.51

(b) Ellipsoid from Raw Outside Measurements. Radii/µT: 45.59, 44.69, 42.37

Figure 4.14.: Ellipsoids Estimated from Measurements in Lab and Outside

Table 4.4.: Radii calculated from data collected outside in a disturbance-free environment.

Algorithm	r_1/µT	r_2/µT	r_3/µT
Raw	45.693	44.456	42.719
Reference	48.609	48.609	48.609
Norm LSM	48.611	48.602	48.595
Ellipsoid	48.609	48.609	48.609

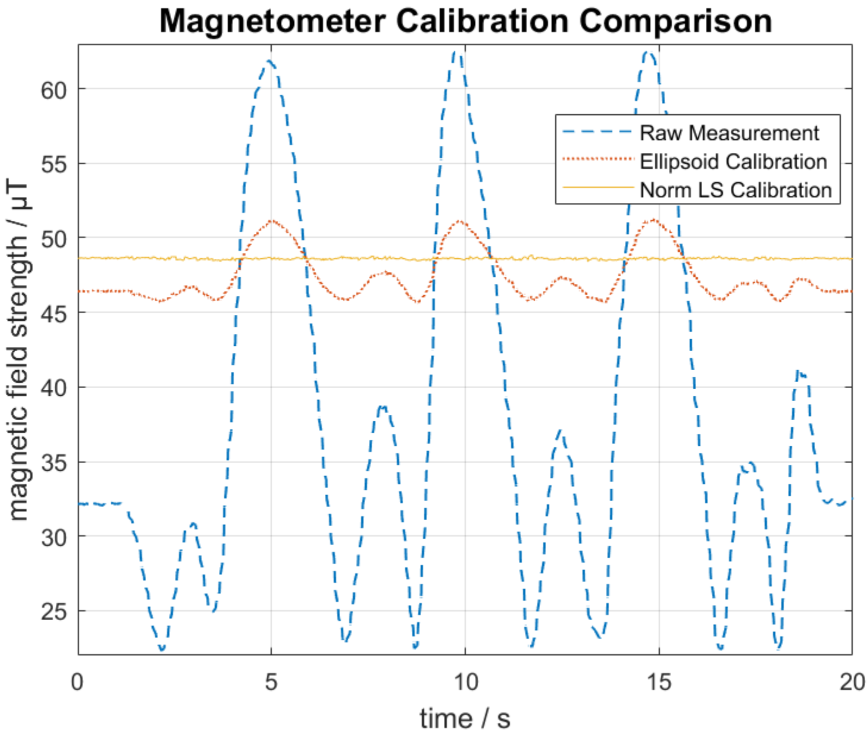

Figure 4.15.: Comparison of Magnetic Field Magnitude of different Calibration Algorithms

strength. Figure 4.15 depicts a comparison of the magnetic field magnitude with respect to time. The field strength of the ellipsoid calibration is shown in dotted red, and the norm least squares algorithm is in solid yellow. Finally, the dashed blue line represents the raw magnetic field intensity. Contrary to the previous finding of more stable radii with the ellipsoid calibration, this plot suggests a constancy of the norm least squares method. The ellipsoid calibration reduces the oscillation amplitude drastically, but a variation in the order of about $\pm 5\,\mu\mathrm{T}$ is still visible. Hence, the norm least squares calibration algorithm scores better in this regard.

Moreover, the ellipsoid calibration algorithm provides very similar parameters when doing the same procedure with different sets of similar data. The least squares algorithm finds distinct solutions when exposed to new measurements. For example, the bias vector for another data set is estimated to be $[-2.0195, -14.6625, -17.8307]^T$ with the least squares method while the ellipsoid calibration estimates $[-5.3618, -8.2111, -17.8364]^T$ which is very similar to the other data set.

Distortions of the natural magnetic field can also contaminate the outside measurements, for example, stemming from the proximity of the person handling the terminal manually. Also, electrical components like phones and the connection to a running computer may influence the data. Moreover, the IGRF model is just a model predicting the magnetic field with limited resolution, and absolute truth cannot be guaranteed. Due to the rotating motion, the terminal's location differed by about ± 15 cm. The model is not as locally precise, and the magnetic field is assumed constant for the movement considering the lateral distance and consumed time. Still, a change in field strength must be considered. In general, an unequivocal verification of the results is impossible with the limited test setup. Both algorithms seem favorable from different perspectives. As they both achieve a reduction of distorted measurements, a performance comparison conducted in the actual mission may yield a more meaningful result.

4.5. Analysis of the Optical Link

After calibrating the sensors, an optical link is implemented with a 1590 nm laser. To simulate an accurate link scenario, the hexapod performs random movements in the range of an absolute of $\pm 1°$ with a velocity of 0.08 dps. The closed control loop adapts the mirror to the movement of the incoming beam to keep the link stable during tumbling. Integration of the imu measurements into the control loop has yet to be accomplished. The Telemetry data of the microcontroller gives info on the mirror movement as an integer value ranging from −65 536 to 65 536. Also, a scale factor of 352 is multiplied, and an offset of 180 is subtracted to calculate the motor's needed voltage, as seen in equation (4.8).

$$\theta_V = \theta_{fsm} * 2 * 2.5 * 72/65536 - 180 \tag{4.8}$$

$$\theta_x = \theta_{x,mech} * 2/7.289 \qquad \theta_y = \theta_{y,mech} * \sqrt{2}/7.289 \tag{4.9}$$

A lookup table for the actuator of the mirror, which can be found in appendix A, can then be used to extrapolate the mechanical angle this voltage provokes. To calculate the optical angle instead of the mechanical one, different scale factors are needed for the x- and y-axis, as can be seen in equation (4.9). This is reasoned by the design of the optical payload. Now, the hexapod, the mirror and the gyroscope data can be compared. To compare the angles, the gyroscope data has to be integrated with respect to time.

$$\varphi(t) = \varphi(t-1) + \int \omega(t)dt \tag{4.10}$$

As equation (4.10) shows, the integrated part is added to the previously known attitude. $\varphi(t)$ is the angle wanted to calculate and $\omega(t)$ denotes the time-dependent angular velocity measured by the gyroscope. Note here that the gyro measurements are discrete in time; therefore, discrete integration algorithms like the *trapz* function in MATLAB must be utilized. A portrayal of the integration with the continuous integration sign has been chosen to represent the mathematical basis. The previous attitude $\varphi(t-1)$ can be understood as the integration constant, and there are two options for fetching these values. Firstly, in a recursive manner and assuming the starting angle to be zero, the previous angle can be determined by integrating prior gyro measurements. A second, less error-prone option is to obtain the angle determined by the satellite's ADCS with its relatively slow update rate (or the real hexapod angle in the lab case) and propagate the angle from that value. This method is less prone to poor results as the propagation error is reset with every new attitude update of the satellite. Therefore, errors will not be accumulated.

The velocities can be calculated from the angles by using the following equation 4.11:

$$\dot{x}(t) = \frac{\partial x}{\partial t} = \frac{x(t) - x(t-1)}{\Delta t} \tag{4.11}$$

In this equation, $x(t)$ is a time-dependent variable with discrete steps. First, the general mathematical style for derivatives with respect to time is used. Then, the discrete formulation of deriving a time-dependent variable is displayed. The calculation of velocities is also not prone to accumulating errors, but large movements in very little time will result in spikes that are not recorded by slow sensing equipment. Therefore, both comparison methods have flaws and will be discussed in the following subsections 4.5.1 and 4.5.2.

4.5.1. Comparison of Angles

As discussed, any slight offset will produce a large value when integrated over a long time. This can be seen in figure 4.16, which presents the angles with respect to time. The FSM and hexapod angles can be observed in dashed blue and dash-dotted black, respectively. The dotted red line shows the integrated gyroscope angles by just utilizing the gyroscope data. As explained before, the hexapod angle can be used as the previous angle. This is implemented in the solid purple plot.

After 300 seconds, the calculated gyroscope angle rises higher than the other angles. As the solid purple graph shows, this could be explained by accumulating noise during integration, which periodic attitude updates can prevent. Another possible explanation is the existence of a bias instability that has yet to be accounted for. Since the gyroscope datasheet does not give any information about bias instability, it can only be speculated to be the result of temperature changes or a time dependency in the sensor bias. This finding complicates the calibration even more, and better solutions than static algorithms should be considered in the future. On the other hand, as the purple graph shows, resetting the previous position with every new update of the satellite's ADCS, the gyro data can provide precise information about the satellite's attitude. Some errors occurred, but considering the implementation in a control loop, the results are promising.

A difference between the blue graph representing the FSM and the graphs of gyro and hexapod can be observed. This might be due to over-compensation of the movement in the control loop. Another possible fault can be seen in the non-linear conversion from voltages into angles via the lookup table. As the blue graph is always located above the other graph, an offset is another possible reason. The FSM has to be at an angle different from zero to acquire a link. Since the bias is not entirely constant, an interplay of all named possible faults seems logical.

4.5.2. Comparison of Velocities

Calculating the derivative is trivial, as shown in equation (4.11). Three different plots can be seen in figure 4.17. The dashed blue line shows the velocity of the mirror received by deriving the angles. Furthermore, gyroscope measurements plotted in dotted red and hexapod velocity also gained by derivation, plotted in solid black, are almost indistinguishable. A low pass filter has been implemented, which helps smooth the FSM velocity graph and makes it much more compatible with the measured gyro velocity. The filter is designed with the *designfilt* command in MATLAB, and a lowpass IIR Filter of order eight is chosen. The passband frequency is determined to be 25 Hz, and the sample rate is set to 200 Hz since the sensors are working with that frequency. A passband ripple option of 5.9 Hz is chosen to best fit the real velocities of the hexapod. Note that the x-axis of the gyroscope and mirror's second axes are plotted here as

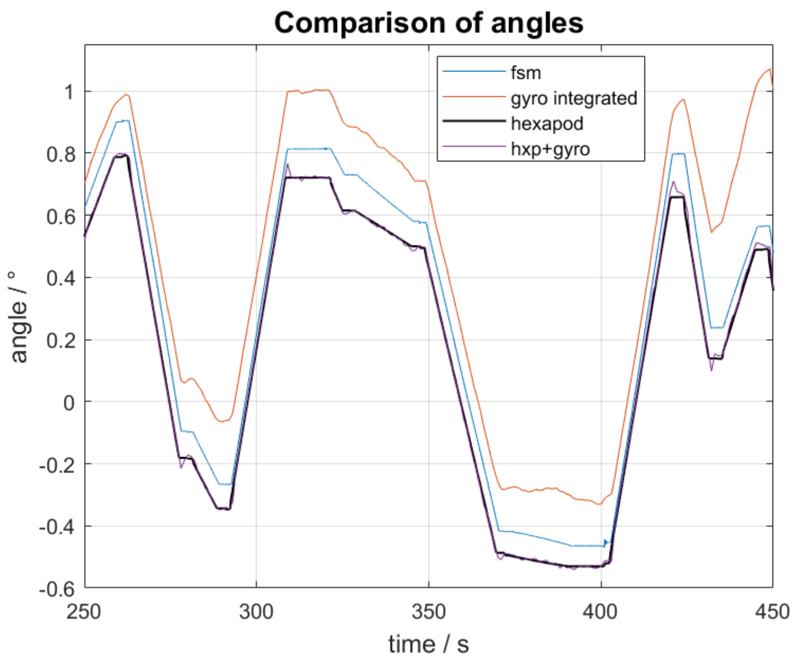

Figure 4.16.: Comparison of Angles

the body frames differ. Section 4.5.3 shows how to account for these differences via the LSM.

Little spikes can also be observed in the hexapod velocities. The command for the motion was *IncrementalMoveWithVelocity*, resulting in a very imprecise movement from the hexapod. A precise absolute move command is used to eradicate this imprecision and end at the requested angles. This is important to ensure no errors will be propagated forward. On the other hand, the movement is conducted with maximum velocity since the velocity cannot be specified with this command. These fast movements can also result in the control loop losing the link. Therefore a spiral starts again, resulting in spikes in the FSM graph, for example, at about 400 seconds. Since the movements are relatively minor, the link is found again quickly, and the mirror does not spiral for a long time.

4.5.3. Rotation Matrix Gyro to FSM

The gyroscope and the fine steering mirror are located on the terminal, but their location and attitude differ, resulting in distinct coordinate systems inherent to each component. To adjust the coordinate systems to each other, a rotation matrix can be determined from the CAD model of the terminal. Also, mounting differences can cause deviations from the predicted attitude difference. A rotation matrix can be computed again using the standard LSM to account for those mounting differences between the mirror and the gyroscope. Since the mirror only has two degrees of freedom and the gyroscope measures all three axes, the dimensions of the rotation matrix are 2×3.

$$\boldsymbol{R}_{t2,g2fsm} = \begin{bmatrix} 0.046 & 0.992 \\ 0.019 & -0.059 \\ 0.960 & -0.044 \end{bmatrix} \qquad \boldsymbol{R}_{CAD} = \begin{bmatrix} 0 & 0 & -1 \\ 0 & -1 & 0 \\ -1 & 0 & 0 \end{bmatrix} \tag{4.12}$$

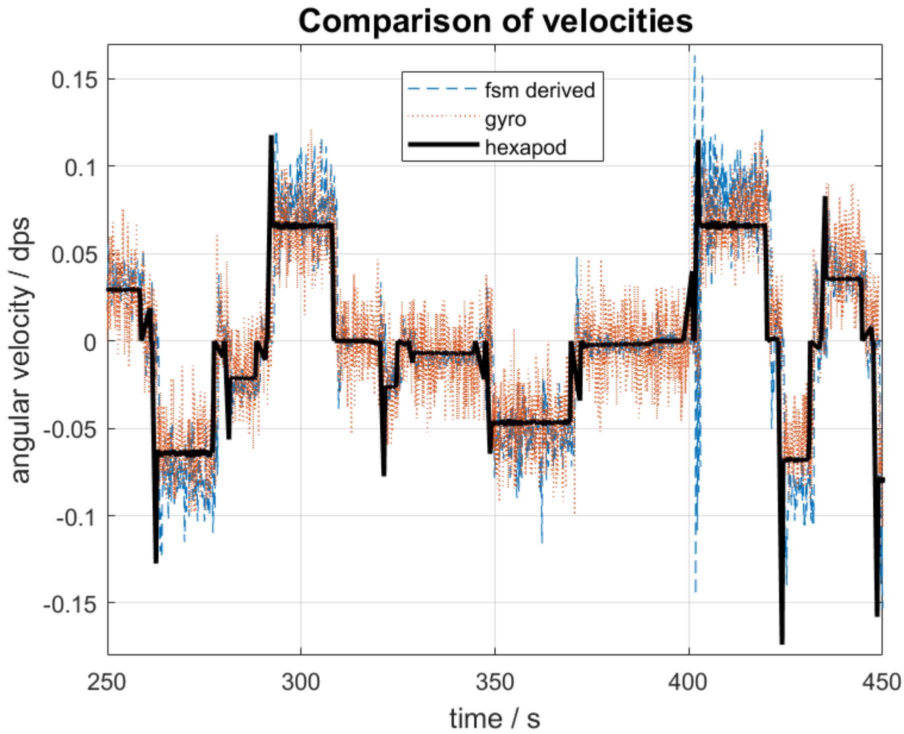

Figure 4.17.: Comparison of the angular velocity derived from hexapod and FSM and measured by the gyroscope. All three match well together, verifying the feasibility of using the gyroscope for gaining additional attitude information.

In equation (4.12), $\boldsymbol{R}_{t2,g2fsm}$ is the least squares estimate of the rotation matrix from gyro to FSM, and $\boldsymbol{R}_{CAD}$ is the rotation matrix according to the model. It can be seen that the gyroscopes' x-axis corresponds to the mirror's second axis and the gyroscopes' z-axis to the mirror's first axis. Also, the norm of this matrix is 0.995; therefore, it can be assumed to be a real rotation matrix that is always normalized.

This result can be verified by comparing it to the CAD model of the terminal. According to the model, the gyroscope axes are rotated by 180° around the x-axis and 90° around the y-axis resulting in an anti-diagonal negative unit matrix. The middle vector can be ignored as the laser looks along the y-axis. Also, the mirror works in the opposite direction of the motion to compensate for it. Hence, opposite signs are applied to the rotation matrix of the mechanical model. The least squares algorithm additionally detects slight mounting differences; therefore, the resulting matrix $\boldsymbol{R}_{t2,g2fsm}$ in equation (4.12) is verified in a qualitative matter. Noise from both sensors again obstructs the resolution of this method. Moreover, a quantitative validation is impossible as the mounting differences are minimal, and measuring methods are limited considering the natural coordinate systems of the components.

Figure 4.18 displays the comparison of the angular velocities after applying the determined rotation matrix. The solid blue line represents the derived FSM velocity, and the dashed red plot shows the rotated gyro measurements. Both graphs are very compatible, with only some spikes showing a deviation. As explained before, the gyroscope spikes around 20 s may stem from a rapid movement conducted by the hexapod. A spiraling movement at around 230 s

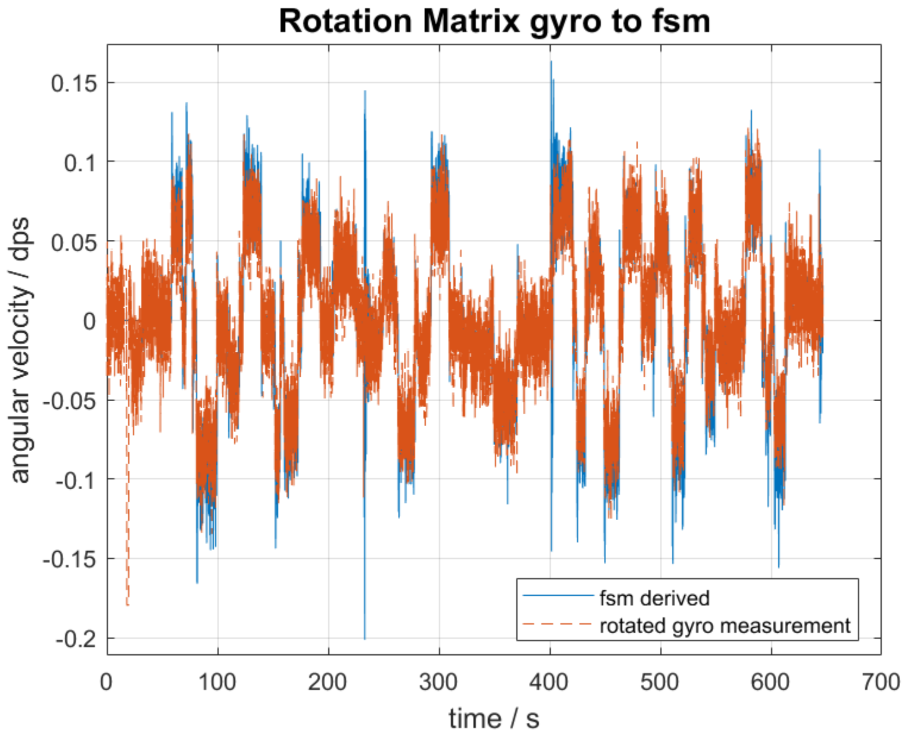

Figure 4.18.: A great fitting of the measured angular velocity to the FSM can be observed after computing the rotation matrix between both body frames.

probably caused large values in the FSM graph. Generally, the FSM seems to move slightly faster than the detected gyroscope velocity, which is explained by the control loop slightly overcompensating the motion.

The determination of this rotation matrix can compensate for the orientation differences between the sensors. Discrepancies between the CAD model and the actual mounting always exist and have to be accounted for. Thus, this algorithm ensures a superior integration of the gyroscope measurements into the mirror's control loop.

5 Chapter 5.
Summary and Outlook

Optical satellite communication is an indispensable and rapidly improving technology. The miniaturization of satellites sparks new opportunities like satellite constellations, creating a vast demand for inter-satellite communication links. For the efficient implementation of lasers, small beam divergences are essential to increase the link budget. In order to ensure beam acquisition, a motorized assembly extends the observable area. Fast and precise attitude information is required to compensate for unforeseen satellite movements. Thus, calibration algorithms for gyroscope and magnetic field sensors have been investigated in this work, providing accurate results.

In the first experiments with the sensors, noise characteristics were examined to determine fitting settings. Sadly, measurements by one gyroscope sensor, the A3G4250, are too noisy to detect angular velocities in the required magnitude scale meaningfully. A gyroscope sensor with less noise but a similarly stable bias would be a great addition to the current setup when considering future terminal iterations. The other sensors yield satisfying results for the mission specifications. However, the scalable, high range on the IAM20380 is not required for the mission; instead, a higher resolution would improve the performance. Then, three different calibration algorithms have been investigated in this work, the standard least squares method, a norm least squares algorithm and an ellipsoid calibration specifically for magnetic field sensors. Following some simulations, testing has been conducted in a lab setup and outside, guaranteeing a more disturbance-free environment. For gyroscope sensors, the standard least squares method obtained the best results. The calibration parameters considering the magnetometer determined by the norm least squares algorithm and the ellipsoid calibration algorithm score similarly and can both be utilized in a low-earth orbit satellite mission. Moreover, a rotation matrix between the gyroscope sensor and the fine steering mirror could be established, guaranteeing a superior control loop. Validating the results proves difficult as no absolute truth or exact reference value is available. Errors may stem from inaccuracies of the testing equipment, namely hexapod, goniometer, turntable and 3D-printed stand. Moreover, the magnetic reference is only modeled with limited accuracy and cannot account for temporary disturbances. Analysis has shown enhanced fitting to given reference values and a satisfactory correction of different errors.[1]

Collectively, the analyses performed contribute to the development of more reliable optical inter-satellite links. Small satellite systems and their communication will likely become increasingly important, providing internet connections in remote areas and secure data transmission. Future project steps will implement an absolute attitude determination algorithm and a Kalman filter for real-time data filtering. When conducting the actual mission, further analysis of both magnetometer calibration methods should be enforced to identify the superior algorithm.

1 All necessary programs were self-written by the author in MATLAB and C and can be provided upon request.

Chapter 6.

6 Bibliography

[1] C. Fuchs and C. Schmidt. “Update on DLR’s OSIRIS program”. In: *International Conference on Space Optics—ICSO 2018*. Vol. 11180. International Society for Optics and Photonics. 2019, p. 111800I.

[2] R. M. Calvo et al. “Optical technologies for very high throughput satellite communications”. In: *Free-Space Laser Communications XXXI*. Vol. 10910. SPIE. 2019, pp. 189–204.

[3] B. Rödiger et al. “Acquisition Concept for Inter-Satellite Communication Terminals on CubeSats”. In: *Small Satellites Systems and Services-The 4S Symposium 2022*. 2022.

[4] B. Rödiger et al. “High data-rate optical communication payload for CubeSats”. In: *Laser Communication and Propagation through the Atmosphere and Oceans IX*. Vol. 11506. SPIE. 2020, pp. 12–24.

[5] R. De, M. P. Abegaonkar, and A. Basu. “Enabling Science With CubeSats—Trends and Prospects”. *IEEE Journal on Miniaturization for Air and Space Systems* 3.4 (2022), pp. 221–231.

[6] E. Kulu. “Satellite constellations-2021 industry survey and trends”. In: *35th Annual Small Satellite Conference*. 2021.

[7] A. U. Chaudhry and H. Yanikomeroglu. “Laser intersatellite links in a starlink constellation: A classification and analysis”. *IEEE Vehicular Technology Magazine* 16.2 (2021), pp. 48–56.

[8] P. Bangert. *Magnetic Attitude Control of Miniature Satellites and its Extension towards Orbit Control using an Electric Propulsion System*. Universität Würzburg, 2019.

[9] W. Ley, K. Wittman, and W. Hallmann. *Handbuch der Raumfahrttechnik*. Carl Hanser Verlag, 2007.

[10] J. Diebel. “Representing attitude: Euler angles, unit quaternions, and rotation vectors”. *Matrix* 58.15-16 (2006), pp. 1–35.

[11] J. R. Wertz. *Spacecraft attitude determination and control*. Vol. 73. Springer Science & Business Media, 2012.

[12] G. Wahba. “A least squares estimate of satellite attitude”. *SIAM review* 7.3 (1965), pp. 409–409.

[13] F. L. Markley and D. Mortari. “Quaternion attitude estimation using vector observations”. *The Journal of the Astronautical Sciences* 48.2 (2000), pp. 359–380.

[14] T. F. Mütsch and M. B. Kowalski. “Space Technology”. In: *Space Technology*. De Gruyter Oldenbourg, 2016.

[15] N. J. Kasdin and D. A. Paley. “Engineering Dynamics”. In: *Engineering Dynamics*. Princeton University Press, 2011.

[16] W. Demtröder. “Statische Magnetfelder”. In: *Experimentalphysik 2*. Springer, 2017, pp. 79–116.

[17] “Magnetic Field in Vacuum”. In: *Electromagnetism*. John Wiley and Sons, Ltd, 2012. Chap. 6, pp. 153–194. ISBN: 9781118562215. DOI: `https://doi-org.ezproxy.uni-giessen.de/10.1002/9781118562215.ch6`.

[18] A. Chulliat et al. “The US/UK world magnetic model for 2020-2025” (2020).

[19] P. Alken et al. “International geomagnetic reference field: the thirteenth generation”. *Earth, Planets and Space* 73.1 (2021), pp. 1–25.

[20] D. Winch et al. “Geomagnetism and Schmidt quasi-normalization”. *Geophysical Journal International* 160.2 (2005), pp. 487–504.

[21] G. Zhanshe et al. “Research development of silicon MEMS gyroscopes: A review”. *Microsystem Technologies* 21.10 (2015), pp. 2053–2066.

[22] H. Din, F. Iqbal, and B. Lee. “Modelling and optimization of single drive 3-axis MEMS gyroscope”. *Microsystem Technologies* 26.9 (2020), pp. 2869–2877.

[23] S. Tumanski. *Handbook of magnetic measurements*. CRC press, 2016.

[24] A. Leuzinger and A. Taylor. “Magneto-inductive technology overview”. *PNI white paper* (2010).

[25] B. Riwanto et al. “Cubesat attitude system calibration and testing”. MA thesis. 2015.

[26] R. E. Kalman. “A new approach to linear filtering and prediction problems” (1960).

[27] E. Dorveaux et al. “Iterative calibration method for inertial and magnetic sensors”. In: *Proceedings of the 48h IEEE Conference on Decision and Control (CDC) held jointly with 2009 28th Chinese Control Conference*. IEEE. 2009, pp. 8296–8303.

[28] H. Din, F. Iqbal, and B. Lee. “Design Approach for Reducing Cross-Axis Sensitivity in a Single-Drive Multi-Axis MEMS Gyroscope”. *Micromachines* 12.8 (2021), p. 902.

[29] H. Abdi et al. “The method of least squares”. *Encyclopedia of measurement and statistics* 1 (2007), pp. 530–532.

[30] D. E. Wells and E. J. Krakiwsky. *The method of least squares*. Vol. 18. Department of Surveying Engineering, University of New Brunswick Fredericton . . ., 1971.

[31] Å. Björck. “Solving linear least squares problems by Gram-Schmidt orthogonalization”. *BIT Numerical Mathematics* 7.1 (1967), pp. 1–21.

[32] W. Gander. “Algorithms for the QR decomposition”. *Res. Rep* 80.02 (1980), pp. 1251–1268.

[33] S. Aslan, S. Niu, and J. Saniie. “FPGA implementation of fast QR decomposition based on givens rotation”. In: *2012 IEEE 55th International Midwest Symposium on Circuits and Systems (MWSCAS)*. IEEE. 2012, pp. 470–473.

[34] Z.-Y. Huang and P.-Y. Tsai. “Efficient implementation of QR decomposition for gigabit MIMO-OFDM systems”. *IEEE Transactions on Circuits and Systems I: Regular Papers* 58.10 (2011), pp. 2531–2542.

[35] Å. Björck. *Numerical methods for least squares problems*. SIAM, 1996.

[36] J. Fang et al. “A novel calibration method of magnetic compass based on ellipsoid fitting”. *IEEE Transactions on Instrumentation and Measurement* 60.6 (2011), pp. 2053–2061.

[37] O. Hazbon et al. “Digital twin concept for aircraft system failure detection and correction”. In: *AIAA Aviation 2019 Forum*. 2019, p. 2887.

Appendix A. Lookup Table FSM

Device Parameters Summary

Device ID : S40919

Actuator Name: A8L2.2

Actuator Mode : Gimbal-less Dual-Axis Quasistatic

Mirror Type: Bonded

Mirror Size : 5.0mm diameter

Mirror Coating : Gold

Maximum Mech. Angle - X Axis [degrees] : 5.1928

Maximum Mech. Angle - Y Axis [degrees] : 5.2236

Maximum Vdifference - X Axis [V] : 169

Maximum Vdifference - Y Axis [V] : 170

Driver Bias Voltage (Vbias) [V] : 90

Maximum Mech. Angle - Coupled Axes [degrees] : 7.5693

Resonant Frequency - X Axis [Hz] : 278

Resonant Frequency - Y Axis [Hz] : 278

Quality Factor - X Axis : 27.4000

Quality Factor - Y Axis : 28.3000

Recommended LPF Cutoff Frequency (6th Order Bessel) [Hz] : 120

Date and Time Report was Created: 06-Mar-2018 at 18:58:9

Static Response

Voltage vs. Mech. Angle - Individual Axes

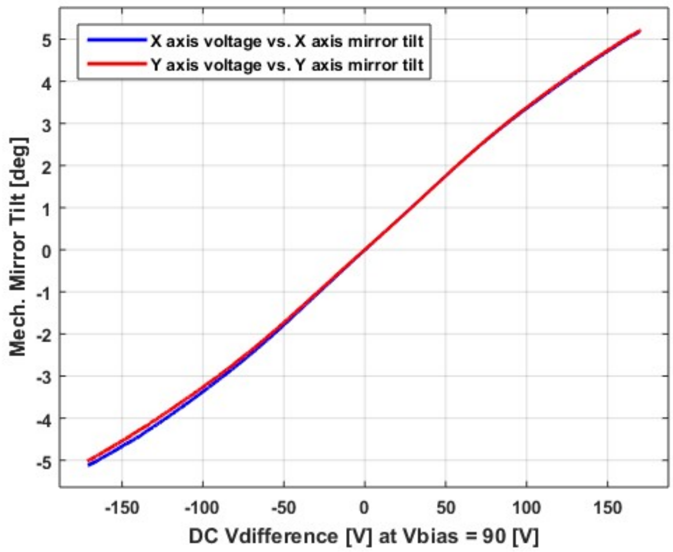

Voltage vs. Mech. Angle - Coupled Axes

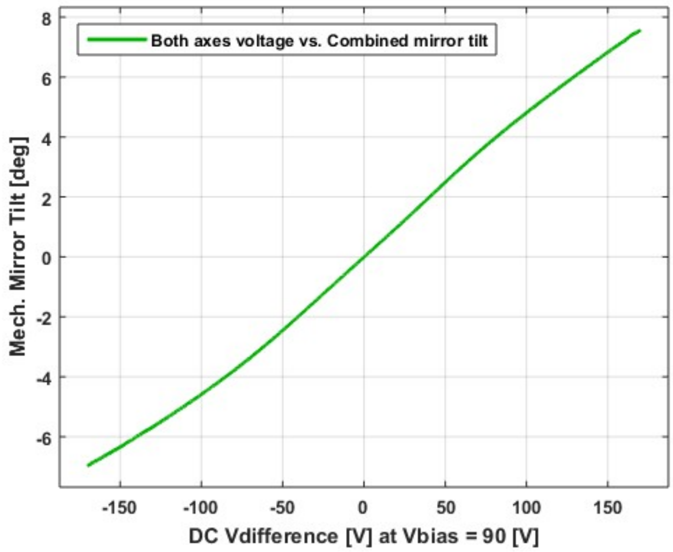

Frequency Response

Small Signal Frequency Response - Magnitude

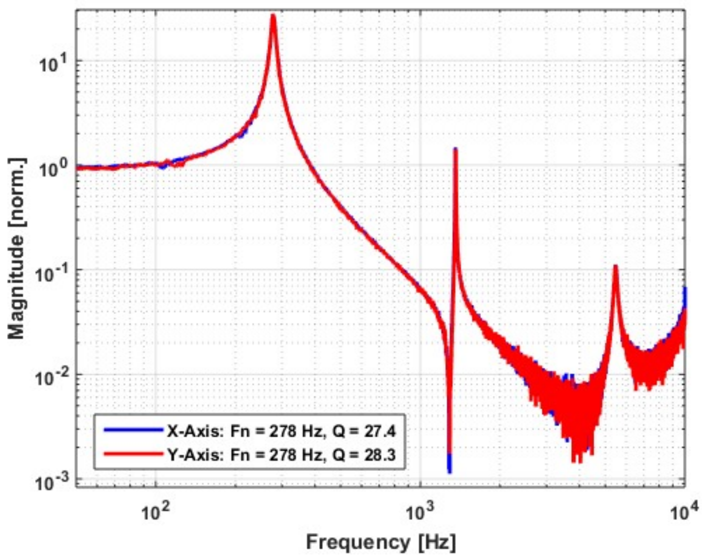

Small Signal Frequency Response - Phase

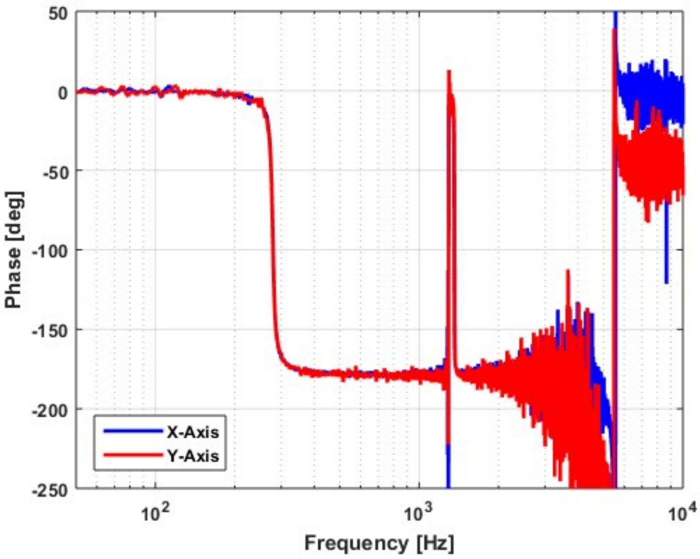

Step Response

X-Axis Step Response

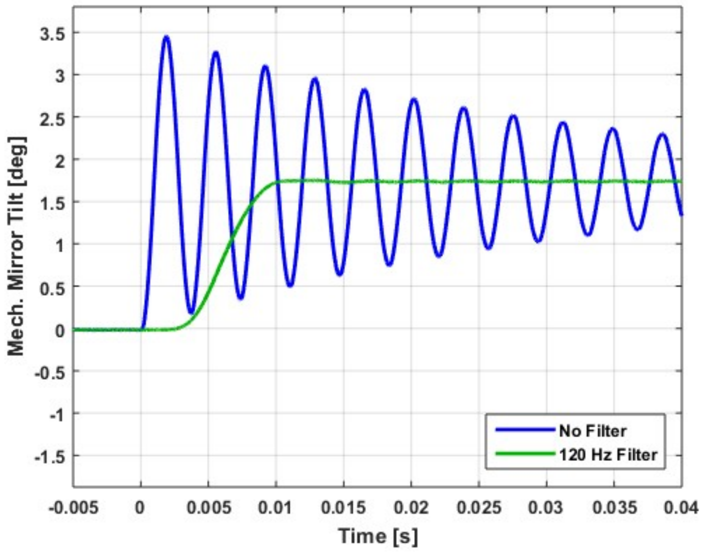

Y-Axis Step Response

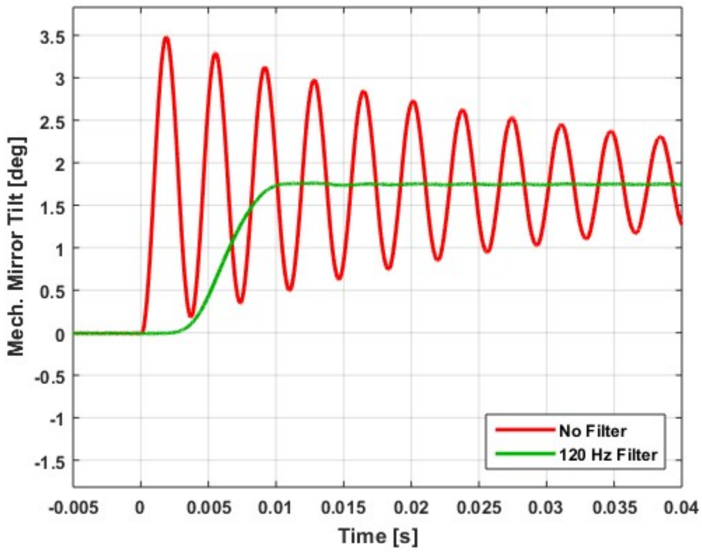

2D Lookup Tables

Voltage vs. X Mech. Angle - Lookup Table

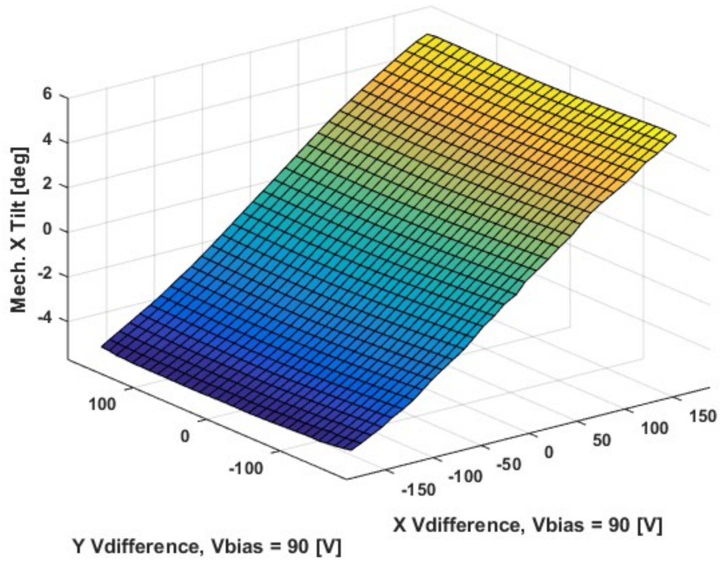

Voltage vs. Y Mech. Angle - Lookup Table

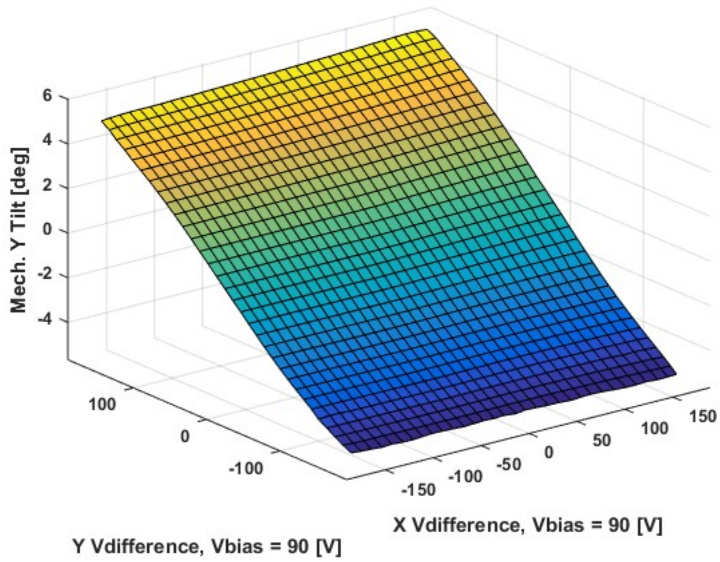

Y vs. X Tilt - Addressable Mech. Angles

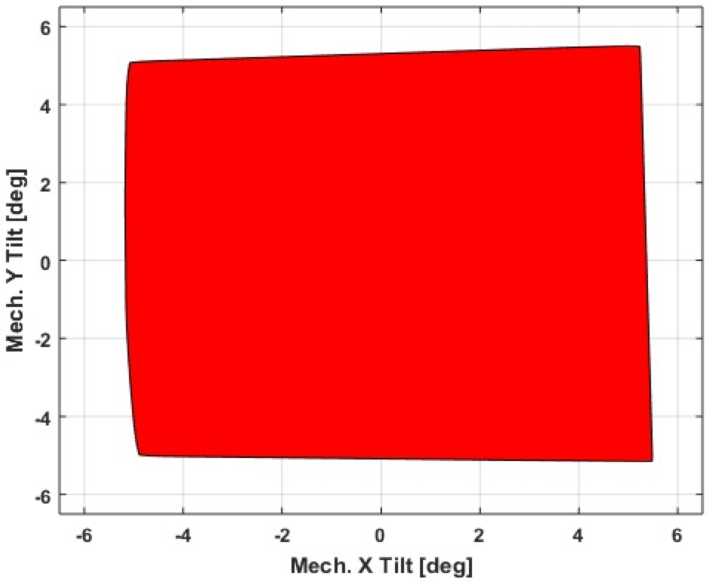

Selbstständigkeitserklärung

Hiermit versichere ich, die vorgelegte Thesis selbstständig und ohne unerlaubte fremde Hilfe und nur mit den Hilfen angefertigt zu haben, die ich in der Thesis angegeben habe. Alle Textstellen, die wörtlich oder sinngemäß aus veröffentlichten Schriften entnommen sind, und alle Angaben die auf mündlichen Auskünften beruhen, sind als solche kenntlich gemacht. Bei den von mir durchgeführten und in der Thesis erwähnten Untersuchungen habe ich die Grundsätze guter wissenschaftlicher Praxis, wie sie in der ‚Satzung der Justus-Liebig-Universität zur Sicherung guter wissenschaftlicher Praxis' niedergelegt sind, eingehalten. Entsprechend § 22 Abs. 2 der Allgemeinen Bestimmungen für modularisierte Studiengänge dulde ich eine Überprüfung der Thesis mittels Anti-Plagiatssoftware.

Datum

Unterschrift